Supplement of Aerosol Research, 4, 231–254, 2026
https://doi.org/10.5194/ar-4-231-2026-supplement

Supplement of

Assessing the sources of submicron airborne elements at two sites in the Fos-Marseille basin through rolling positive matrix factorization

Mathilde Brezins et al.

Correspondence to: Benjamin Chazeau (benjamin.chazeau@univ-amu.fr)
and Barbara D'Anna (barbara.danna@univ-amu.fr)

Detection Limits for Xact 625i – Cooper Environmental Services

Xact 625i Minimum Detection Limits
(ng m^{-3})
For larger spot size
68%Confidence Level ($C_{1\sigma}$) per US EPA IO3.3 and Currie *

Element (At. No.)	Atomic Number	Sampling/Analysis Time (min)					
		15	30	60	120	180	240
Al (13)	13	1500	500	170	61	33	22
Si (14)	14	260	89	31	11	5.9	3.8
P (15)	15	76	26	9.0	3.2	1.7	1.1
S (16)	16	46	16	5.5	1.9	1.0	0.68
Cl (17)	17	25	8.6	3.0	1.1	0.57	0.37
K (19)	19	17	5.8	2.0	0.71	0.39	0.25
Ca (20)	20	4.4	1.5	0.52	0.18	0.099	0.064
Ti (22)	22	2.3	0.79	0.28	0.097	0.053	0.034
V (23)	23	1.7	0.60	0.21	0.073	0.040	0.026
Cr (24)	24	1.7	0.58	0.20	0.071	0.038	0.025
Mn (25)	25	2.1	0.71	0.25	0.087	0.047	0.031
Fe (26)	26	2.5	0.85	0.30	0.11	0.057	0.037
Co (27)	27	2.0	0.68	0.24	0.085	0.046	0.030
Ni (28)	28	1.4	0.47	0.17	0.059	0.032	0.021
Cu (29)	29	1.1	0.39	0.14	0.048	0.026	0.017
Zn (30)	30	0.95	0.33	0.12	0.041	0.022	0.014
Ga (31)	31	0.83	0.29	0.10	0.036	0.019	0.013
Ge (32)	32	0.79	0.28	0.097	0.034	0.019	0.012
As (33)	33	0.90	0.31	0.11	0.039	0.021	0.014
Se (34)	34	1.2	0.40	0.14	0.050	0.027	0.018
Br (35)	35	1.5	0.52	0.18	0.064	0.035	0.023
Rb (37)	37	2.7	0.95	0.33	0.12	0.064	0.042
Sr (38)	38	3.1	1.1	0.38	0.13	0.072	0.047
Y (39)	39	3.9	1.4	0.48	0.17	0.092	0.060
Zr (40)	40	4.7	1.6	0.57	0.20	0.11	0.071

Nb (41)	**41**	**5.8**	**2.0**	**0.70**	**0.25**	**0.13**	**0.088**
Pd (46)	**46**	**31**	**11**	**3.8**	**1.3**	**0.73**	**0.48**
Ag (47)	**47**	**27**	**9.5**	**3.3**	**1.2**	**0.64**	**0.42**
Cd (48)	**48**	**36**	**12**	**4.4**	**1.5**	**0.84**	**0.54**
In (49)	**49**	**44**	**15**	**5.4**	**1.9**	**1.0**	**0.67**
Sn (50)	**50**	**58**	**20**	**7.1**	**2.5**	**1.4**	**0.88**
Sb (51)	**51**	**73**	**26**	**9.0**	**3.2**	**1.7**	**1.11**
I (53)	**53**		**1.4**	**0.49**			
Ba (56)	**56**	**5.7**	**1.9**	**0.67**	**0.24**	**0.13**	**0.083**
Pt (78)	**78**	**1.7**	**0.58**	**0.20**	**0.072**	**0.039**	**0.025**
Au (79)	**79**	**1.4**	**0.50**	**0.18**	**0.062**	**0.034**	**0.022**
Hg (80)	**80**	**1.7**	**0.60**	**0.21**	**0.074**	**0.040**	**0.026**
Tl (81)	**81**	**1.7**	**0.57**	**0.20**	**0.071**	**0.039**	**0.025**
Pb (82)	**82**	**1.8**	**0.63**	**0.22**	**0.078**	**0.042**	**0.027**
Bi (83)	**83**	**1.8**	**0.64**	**0.23**	**0.080**	**0.043**	**0.028**

Table S1: Xact 625i Minimum Detection Limits (ng m^{-3}) for larger spot size at 68% Confidence Level, as given by the constructor

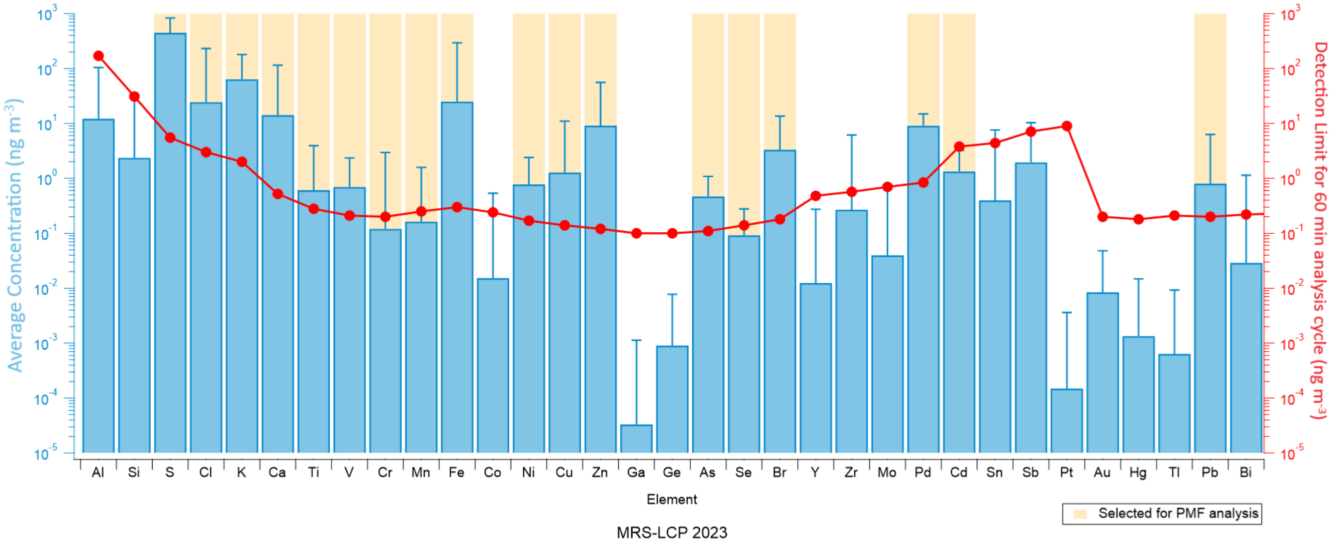

Figure S1: Average concentrations of elements in PM₁ over the entire campaign at MRS-LCP. The red dotted line represents the Xact 625i MDL for 60-minute sampling intervals, while the error bars indicate the standard deviation. Yellow-shaded areas highlight the elements selected for PMF analysis.

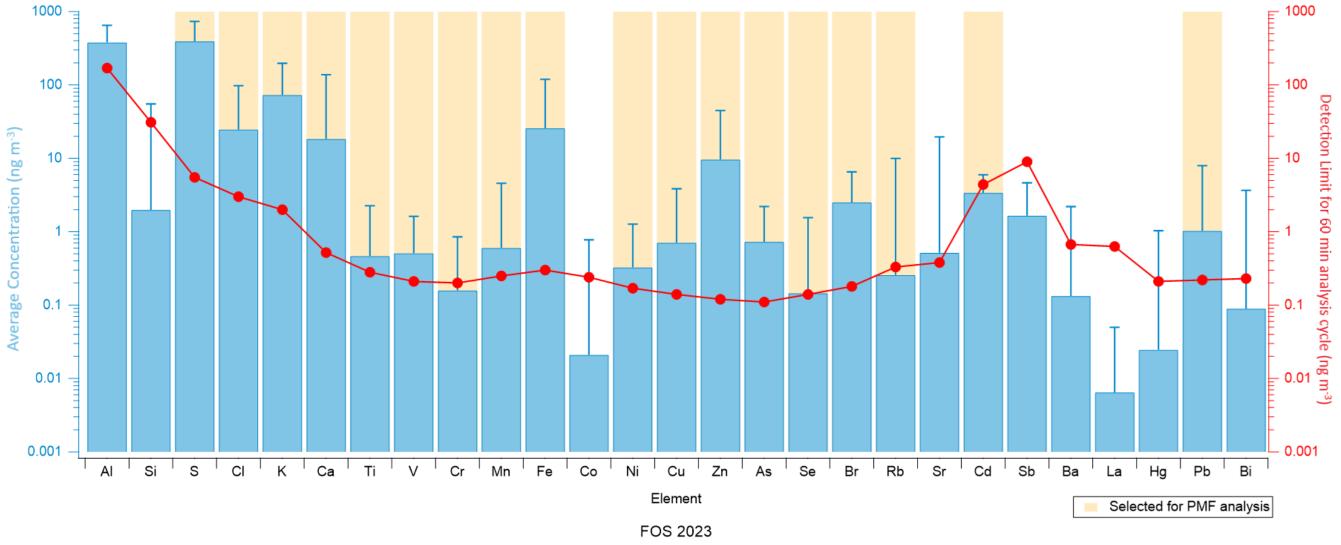

Figure S2: Average concentrations of elements in PM_1 over the entire campaign at FOS. The red dotted line represents the Xact 625i MDL for 60-minute sampling intervals, while the error bars indicate the standard deviation. Yellow-shaded areas highlight the elements selected for PMF analysis.

S1: PMF methodology

Positive Matrix Factorization (PMF) is a powerful bilinear receptor model that describes multivariate datasets as a linear combination of factors (Paatero & Tapper, 1994). Several receptor models allow for quantitative PM source apportionment (Viana et al., 2008), but PMF has been extensively used for this purpose (Reff et al., 2007; Hopke et al., 2020). Unlike Chemical Mass Balance (CMB) model, PMF requires little prior knowledge of the factors involved. In contrast to Principal Component Analysis (PCA), which imposes orthogonality of factors, PMF requires non-negativity, making it particularly suitable for environmental and chemical components analysis. The bilinear factor analytic model is defined as:

$$(\text{S1})\ x_{ij} = \sum_{k=1}^{p} g_{ik} \,.\, f_{kj} + e_{ij}$$

Where x_{ij} is the measurement term, g_{ik} is the factor time series, f_{kj} is the factor profile, and e_{ij} is the model residual. The indices *i*, *j*, *k*, and *p* correspond to the time elements, variables, factor numbers, and the total number of selected factors, respectively.

To solve Equation (S1), the PMF solver fits the non-negative entries in g_{ik} and f_{kj} using a least squares algorithm to iteratively minimise the objective function *Q*, defined as:

$$(\text{S2})\ Q = \sum_i \sum_j \left(\frac{e_{ij}}{\sigma_{ij}}\right)^2$$

Where e_{ij} is the residual element and σ_{ij} is the measurement uncertainty for data point ij. Data points where $e_{ij} \gg \sigma_{ij}$ contribute significantly to Q and may impact the modeling. To prevent the model from being destabilized by a few outliers with high residuals and low uncertainties, the model is run in "robust" mode (Paatero, 1997), where outliers are defined as:

$$\text{(S3)} \left|\frac{e_{ij}}{\sigma_{ij}}\right| > \alpha$$

A value of α = 4 is recommended by Paatero (1997) for the "robust" mode. Outliers are then dynamically reweighted to reduce the dependence of Q on the changes in outlier residuals. To examine the objective function Q across different PMF runs, the ration Q/Q_{exp} is calculated where Q_{exp} represents the degree of freedom of the model solution, with:

$$\text{(S4)}\ Q_{exp} = n.m - p.(m+n)$$

Where n is the number of time points, m is the number of variables, and p is the number of factors used in the PMF run. The ratio Q/Q_{exp} has been reported to have a high variability, ranging from values below 1 to over 30 in previous studies (Brown et al., 2015; Belis et al., 2019; Canonaco et al., 2021; Manousakas et al., 2022; Via et al., 2022), depending on the instrument used and on the measured and modeled uncertainties. While an ideal value of Q/Q_{exp} is close to 1, its absolute value cannot be used as a sole metric for judging model results. Instead, one should assess the relative change in Q/Q_{exp} across different model runs to select a reasonable model solution, for instance following the Elbow method. A significant decrease in Q/Q_{exp} typically indicates improved data explanation, while minimal changes suggest that additional factors do not contribute meaningful information, implying that a smaller p is sufficient.

Following the recommendations of Paatero and Hopke (2003), a step function should be applied to remove variables with a signal-to-noise ratio (S2N) less than 0.2, classified as "bad" variables, and downweight those with S2N between 0.2 and 2, classified as "weak" variables. However, this method downweights entire variables, potentially excluding data with low average S2N but some high S2N data points. Therefore, data are downweighted cell-wise according to the method proposed by Visser et al. (2015b): entries in x_{ij} with a signal-to-noise ratio below 2 are downweighted by replacing the corresponding σ_{ij} with $\frac{2}{SNR_{ij}}$.

Different solvers exist for PMF, namely PMF2 and the ME-2 solver. The ME-2 solver has the advantage of improved control over rotational ambiguity, which occurs when multiple mathematically equivalent solutions exist for the same Q value (Paatero, 1999; Paatero et al., 2002). With ME-2 solver, the user can add a priori information into the model (e.g., source profiles), so that it does not rotate and it provides a rather unique solution (Paatero and Hopke, 2009). By incorporating a priori information (e.g., fixed or constrained source profiles or time series), ME-2 can guide the model toward more interpretable and environmentally reasonable solutions (Paatero and Hopke, 2009). One widely used technique to constrain the solution space is the *a-value* approach, where selected factor profiles or factor times series are constrained using anchor values, and the scalar a defines the extent to which the outputs f'_{kj} or g'_{ik} are allowed to vary during model iteration.

$$\text{(S5)}\ f_{kj} = f'_{kj} \pm a.f_{kj}'$$

$$\text{(S6)}\ g_{ik} = g_{ik}' \pm a.g_{ik}'$$

With the index j representing the variable and i the measured point in time for the k-th factor. Statistical uncertainties and rotational ambiguity of the PMF solutions were assessed using a bootstrap resampling approach (Efron, 1979; Ulbrich et al., 2009) and, for constrained solutions, by varying randomly the a-value. Bootstrap resampling technique consists of generating a number of new PMF input matrix, whose length are generally from a few days to 2 months, with randomly selected timepoints. If the bootstrapped PMF results remain consistent across these perturbed datasets, the solution is considered statistically robust. The variability observed among bootstrap runs within the same factor is then interpreted as the statistical uncertainty of that factor.

S2: PD-SID

The Pearson Distance (PD, Belis et al., 2015; Pernigotti et al., 2016; Pernigotti & Belis, 2018) is equal to $1 - r^2$ where r^2 is the Pearson coefficient. As PD is sensitive to outliers, in this study it is particularly influenced by elements that dominate the composition of each factor, i.e. the most abundant species such as S, K, Ca, or Fe.

SID is defined by:

$$SID = \frac{\sqrt{2}}{m}\sum_{j=1}^{m}\frac{\left|x_j - y_j\right|}{x_j + y_j}$$

with x_j and y_j the relative contribution of the specie j to the x and y factors, and m the number of common species in x and y. $PD < 0.4$ and $SID < 1$ are considered as acceptable criteria for chemical homogeneous profiles.

S3: Cosine Distance

The Cosine Distance is equal to $1 - cosine\ score$ where $cosine\ score$ is defined by:

$$cosine\ score = cos(\theta) = \frac{x\,.\,y}{\|x\|.\,\|y\|}$$

Where x and y are 2 different factors (Stein & Scott, 1994). The $cosine\ score$ is analogous to the Pearson correlation coefficient but has the advantage of being less sensitive to outliers. For this reason, it has previously been used to assess profile similarity in aerosol mass spectrometric data (Ulbrich et al., 2009).

S4: PM$_1$ Mass Reconstruction at MRS-LCP

Direct PM$_1$ mass concentrations obtained with the FIDAS 200 instrument are limited to particles larger than 180 nm. However, a significant fraction of fine particles, particularly those of anthropogenic origin from combustion processes, lies below 200 nm (Manigrasso et al., 2022). To account for this limitation, PM$_1$ mass concentrations at MRS-LCP were reconstructed using two complementary methods: summing the mass contributions from PM$_1$ chemical species obtained through the ToF-ACSM and Xact Rolling PMF, as well as deconvoluted BC_{SF} and BC_{LF} from AE33, and deriving PM_1 mass from the submicronic particle size number distribution measured by the SMPS (15nm-723 nm size resolution), following the approach of Heutte et al. (2023) or using an average aerosol density of 1.5 g cm^{-3}. Reconstruction with specific particle densities yielded results nearly identical to those using the average density ($R^2 = 0.99$, b = 0.97; Figure S3a), and thus the specific particles density approach was adopted as the reference for PM_1 mass from SMPS in subsequent analyses. Comparison between SMPS-derived PM_1 and FIDAS measurements indicated a slight underestimation by the latter ($R^2 = 0.79$, b = 0.89; Figure S3b). An even larger underestimation was observed when reconstructing PM_1 mass from ToF-ACSM and Xact Rolling PMF results, and BC_{SF} and BC_{LF} from AE33 ($R^2 = 0.75$, b = 0.75; Figure S3c). The latest indicates that SMPS-derived PM_1 mass is more reliable, which is consistent with the higher collection efficiency of the SMPS for ultrafine particles (<100 nm). Consequently, PM_1 mass from SMPS was used for comparison with total elemental mass from Xact (Figure S4), showing that airborne elements accounted for ~8% of PM_1 mass on average. Notably, Xact elements contribute slightly more to PM_1 mass during summer, reflecting increased sulfur levels.

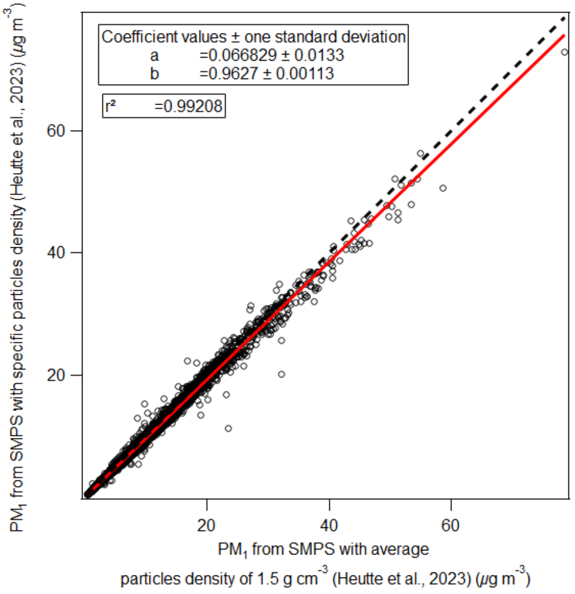

a)

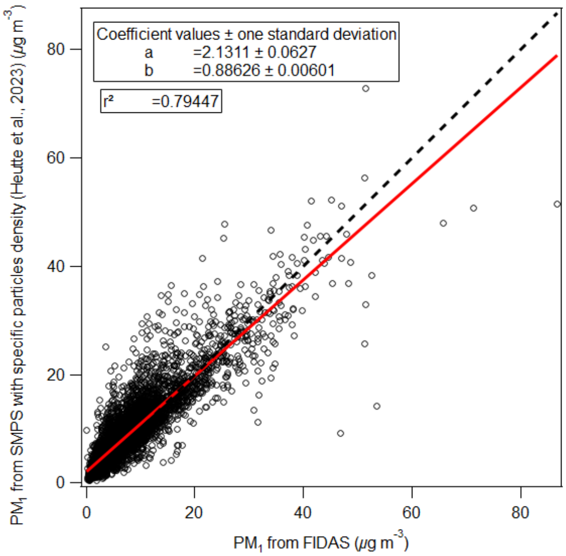

b)

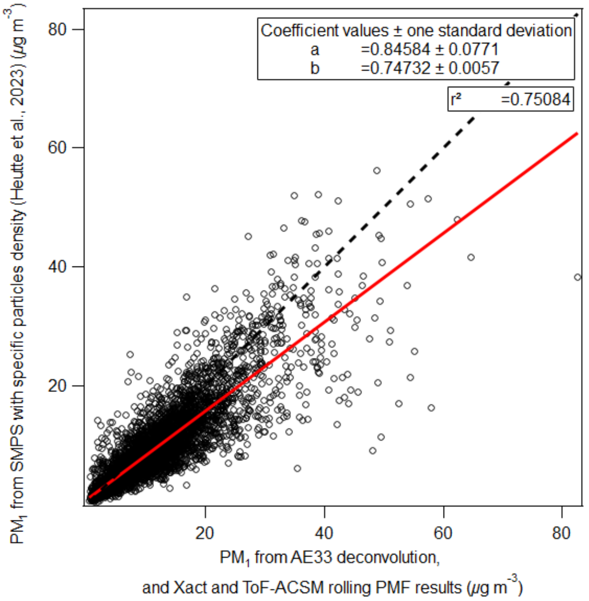

c)

Figure S3: Linear correlation of the PM$_1$ concentration reconstructed from SMPS data with specific particles density (Heutte at al., 2023) versus a) PM$_1$ mass from SMPS with average particles density (1.5 g cm^{-3}), b) PM$_1$ from FIDAS, and c) PM$_1$ from ToF-ACSM and Xact Rolling PMF results, and BC$_{SF}$ and BC$_{LF}$ from AE33, at MRS-LCP.

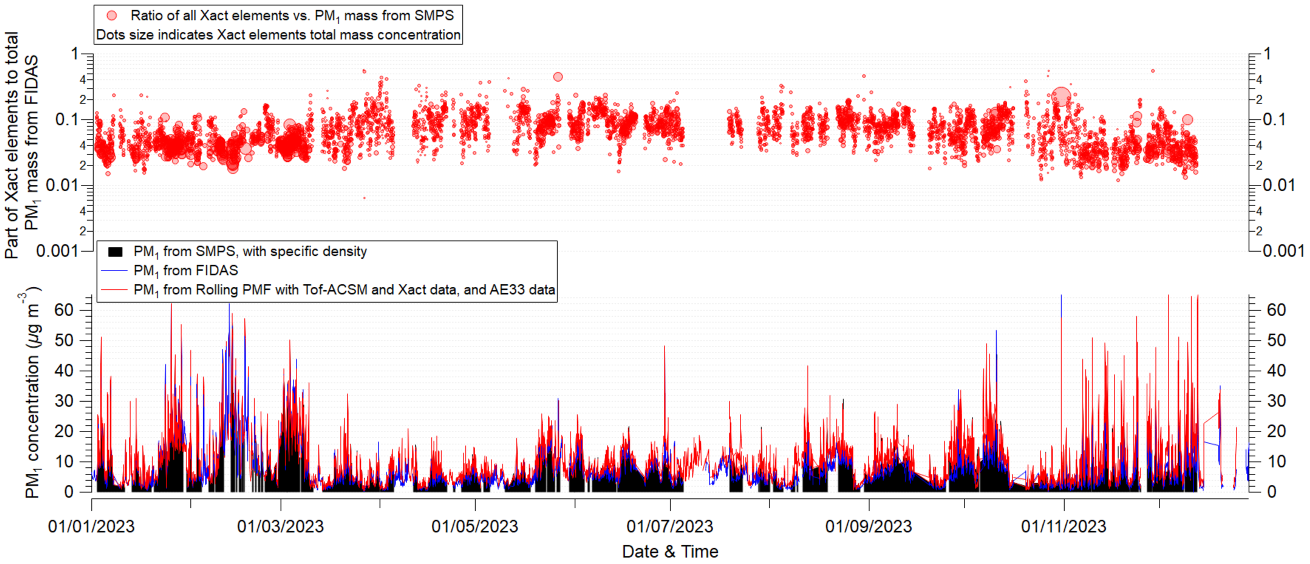

Figure S4: PM$_1$ concentration derived from different methods explained above, and ratio of total elements from Xact versus PM$_1$ derived from SMPS, at MRS-LCP for 2023.

Metal	LOD (ng m^{-3})	BDL (%)

K	2,00	0,01
Zn	0,12	0,01
S	5,50	0,06
Fe	0,30	0,13
Br	0,18	2,82
Ca	0,52	9,53
Cu	0,14	11,84
Pd	3,80	19,15
Ni	0,17	26,20
As	0,11	39,74
Ti	0,28	44,17
Cl	3,00	54,19
V	0,21	56,05
Se	0,14	77,54
Pb	0,22	82,29
Mn	0,25	90,83
Cd	4,40	92,67
Cr	0,20	94,63

Table S2: Xact 625i Minimum Detection Limits (ng m^{-3}) and percentage (%) of data Below Detection Limit (BDL) for each selected element at MRS-LCP

Metal	**LOD (ng m^{-3})**	**BDL (%)**
Zn	0,12	0,00
S	5,50	0,20
Fe	0,30	0,57
K	2,00	1,02
Br	0,18	4,55
Ca	0,52	10,87
Cl	3,00	29,28
As	0,11	30,43
Cu	0,14	44,54

Ti	0,28	54,85
V	0,21	64,27
Cd	4,40	68,93
Ni	0,17	71,10
Pb	0,22	72,88
Se	0,14	73,71
Mn	0,25	84,22
Cr	0,20	88,00
Rb	0,33	96,35

Table S3: Xact 625i Minimum Detection Limits (ng m^{-3}) and percentage (%) of data Below Detection Limit (BDL) for each selected element at FOS

S5: Data correction

Both MRS-LCP and FOS monitoring stations are occasionally influenced by sporadic events such as Saharan dust episodes with Sirocco wind, local construction activities, and firework (e.g., National Day on July 14th, Carnival Day on May 6th, and the *Olympique de Marseille* official football club 30th Anniversary Victory Celebration on May 26th). Fireworks can be readily identified by the specific gunpowder tracer, Bi (Rai et al., 2020). However, due to variations in chemical composition depending on firework colors, no distinct global firework factor could be resolved in the PMF analysis. Retaining these elements would only produce occasional firework-related spikes across several PMF factors, including Biomass Burning (4.2.2). Therefore, these occasional firework spikes, identified through unusual spikes in Bi as well as K, Cu and Cl, were removed from the dataset.

Although Saharan dust is predominantly found in the coarse fraction, significant enrichment in the fine fraction for Si, Ti, Ca, and Fe has been observed during Sirocco episodes. This fine-fraction enrichment can bias source apportionment analyses using Non-Parametric Wind Regression (NWR), particularly for sources with similar elemental signatures at different locations (e.g., Ca from north-westerly Mistral dust versus south-easterly Saharan dust, or Fe from Steel Industry and Saharan dust; Sections 4.2.4 and 4.2.10). Saharan dust events were identified based on multiple criteria: AtmoSud air quality alerts, wind force and direction, anomalies in daily average temperature relative to a 10-day moving average, elevated PM_{10}/PM_1 ratios, and elevated trace levels of Si, Ca, Fe, and Ti measured by the Xact instrument. Attempts were made to isolate a Saharan dust-related factor using Positive Matrix Factorization (PMF) by including Si as a Saharan dust tracer. However, this approach proved unsatisfactory as Si concentrations in the fine fraction were below detection limits 99% of the year (See Supplements Figures S1 & S2), and the resulting Saharan dust-related PMF factor did not differ significantly in composition from the general Dust factor. Owing to these limitations, Saharan dust-influenced periods were excluded from the dataset.

Building work events (3 events during the year), identified by high spikes of Ca, Fe, Ti and Si during working hours, 8 a.m. to 6 p.m. on working days, have also been removed.

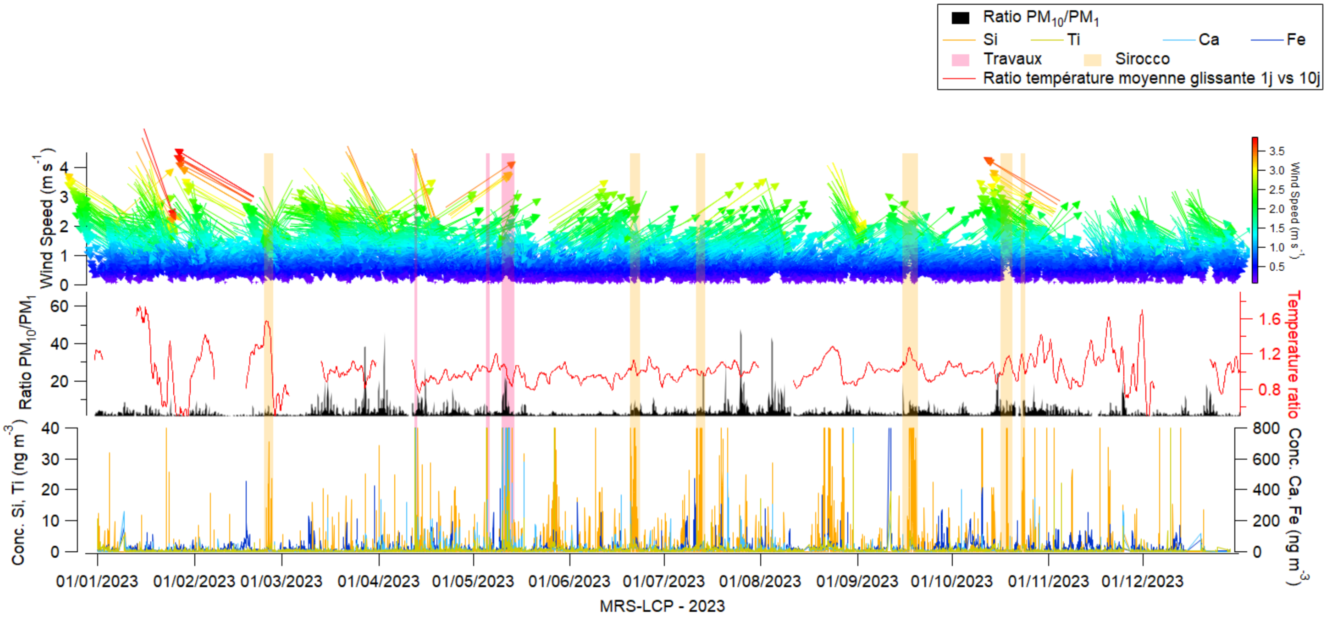

Figure S5: Identification of different dust events during 2023 at MRS-LCP through analysis of wind speed and direction, temperature, PM_{10}/PM_1 ratio, and specific airborne elements concentration.

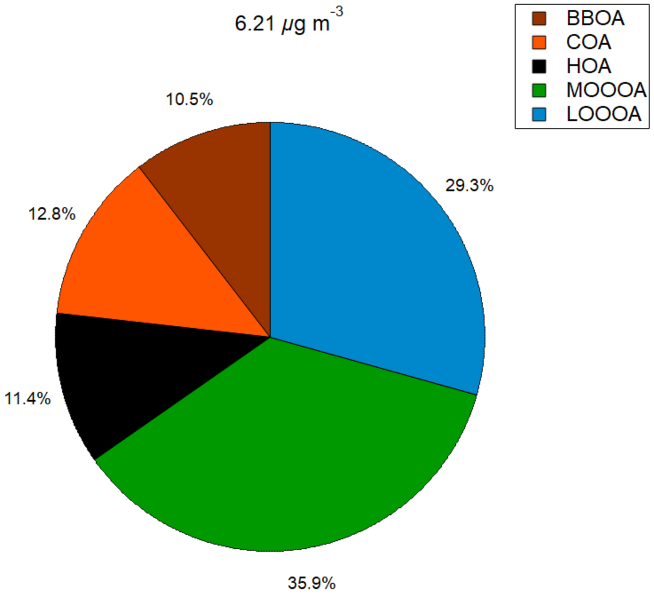

Figure S6: Pie chart showing the mass contribution of Rolling ToF-ACSM PMF factors, for MRS-LCP (2023).

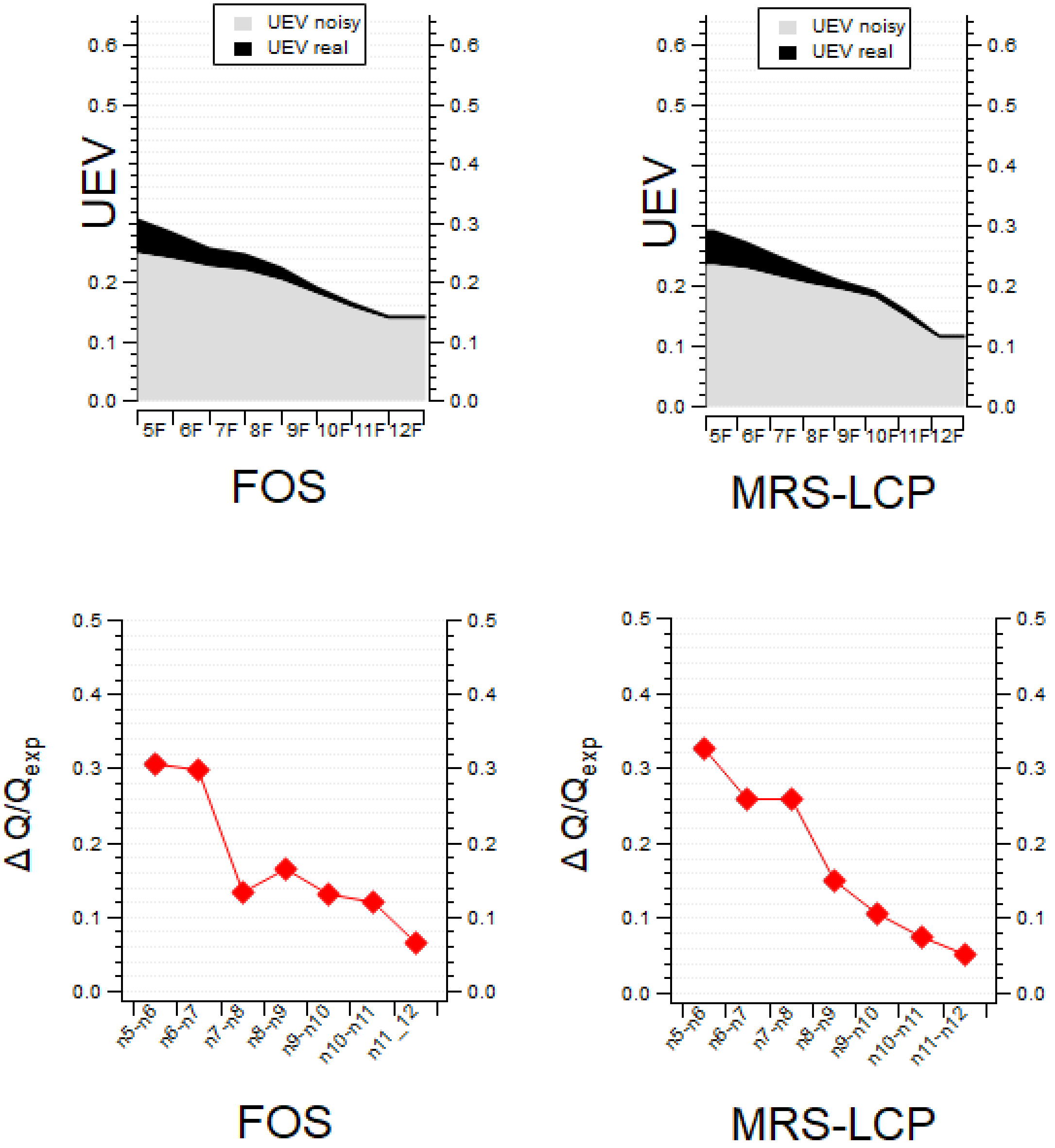

Figure S7: UEV (top) and ΔQ/Q$_{exp}$ (bottom) for unconstrained PMF solutions ranging from 5 to 12 factors, at MRS-LCP (left) and FOS (right). The solutions were repeated 5 times, and the means are displayed in the graphs.

	Composition	**Seasonnality**	**Daily Cycles**	**Geographical origin**	**Correlation with external data**	**Mixing with other factors**	**Previous observations of similar factors in the litterature**
Shipping	S with tracers V & Ni	Mostly during summer with sea breezes	Spikes in the morning and in the evening	Sea (S-W MRS-LCP & S-S-E FOS)	-	Mixed with S-rich (S, Se) below 8 factors	Camman et al., 2024, Fossum et al., 2024
Br-rich	Br	-	-	-	-	-	Camman et al., 2024
Zn-rich (MRS-LCP only)	Mainly Zn, Pb traces	-	-	-	-	-	-
Zn-Industrial (FOS only)	Mainly Zn, Mn traces	-	-	-	-	-	-
Cl-rich	Cl mainly	Mostly during winter	Similar to Biomass Burning diurnal cycle	-	-	Mixed with Biomass Burning (K) below 7 factors	Visser et al., 2015b
Dust	Ca & Ti association	-	Elevated activity during the day	-	-	-	Manousakas et al., 2022
Steel Industry	Mn & Fe association	-	Elevated activity during the day	-	-	-	-

Biomass Burning	Major K contribution	Mostly during winter	Biomass Burning typical cycle	N-E with land breeze, relatively low wind speed	BBOA (ToF-ACSM, MRS-LCP only), BC_{SF} (AE33), Benzene (VOC72M, FOS only)	Mixed with Cl-rich (Cl) below 7 factors	Manousakas et al., 2022
S-rich	S & Se association	Less activity during winter	Flat with slight peak at mid-day	Mainly the sea (S-W MRS-LCP & S-S-E FOS)	SO_4^{2-} (ToF-ACSM, MRS-LCP only)	Mixed with Shipping (V, Ni) below 8 factors	Manousakas et al., 2022
Pb-Industrial (FOS only)	S, K, tracers as Pb	-	-	Distinct geographical origin from both Fos-sur-Mer and Port-de-Bouc industrial complex	-	Below 9 factors, mixed with Biomass Burning	-

Table S4: Table of geochemical criteria for factors identification into preliminary PMF tests, at MRS-LCP and FOS.

Factor	**YEAR**	**JF_D**	**MAM**	**JJA**	**SON**
Shipping	80%	0%	100%	100%	70%
Br-rich	80%	100%	90%	60%	60%
Zn-rich	80%	30%	70%	70%	80%
Cl-rich	80%	30%	70%	0%	80%
Dust	80%	100%	70%	0%	100%
Steel Industry	80%	100%	50%	60%	100%
Biomass Burning	80%	100%	70%	100%	80%
S-rich	80%	0%	100%	100%	70%

Percentage of selected runs among the 10 runs	**80%**	**100%**	**70%**	**100%**	**80%**

Table S5: Results of the preliminary PMF runs at MRS-LCP, showing the percentage of each factor retrieved across five different time periods (YEAR, JF_D, MAM, JJA, SON). Each PMF run was unconstrained, with 10 repeats and 8 factors. Reasonable PMF solutions were analysed through Q/Q$_{exp}$ variations. Red-bordered cells indicate the optimal period for the corresponding factor observation.

Factor	**YEAR**	**JF_D**	**MAM**	**JJA**	**SON**
Shipping	60%	0%	70%	100%	50%
Br-rich	100%	100%	70%	60%	100%
Zn Industrial	100%	100%	100%	60%	100%
Pb-Industrial	100%	100%	100%	100%	100%
Cl-rich	100%	100%	100%	60%	100%
Dust	100%	100%	100%	60%	100%
Steel Industry	100%	100%	100%	60%	90%
Biomass Burning	100%	100%	100%	100%	100%
S-rich	60%	0%	100%	100%	100%
Percentage of selected runs among the 10 runs	**100%**	**100%**	**90%**	**60%**	**100%**

Table S6: Results of the preliminary PMF runs at FOS, showing the percentage of each factor retrieved across five different time periods (YEAR, JF_D, MAM, JJA, SON). Each PMF run was unconstrained, with 10 repeats and 8 factors. Reasonable PMF solutions were analysed through Q/Q$_{exp}$ variations. Red-bordered cells indicate the optimal period for the corresponding factor observation.

MRS-LCP						
Factor	**Criteria position**	**Constrain**	**Criterion**	**SoFi Criterion traduction**	**Static PMF Threshold**	**Rolling PMF Threshold**
Shipping	0	X	Proportion of V apportioned to the factor	factor_1[V]' / sum_[V]'	from 0,66 to 0,92	Score > score of 2nd highest factor

Br-related	1		Proportion of Br apportioned to the factor	factor_2[Br]' / sum_[Br]'	from 0,67 to 0,81	Additional threshold from 0,3 to 1
Zn-industrial	2		Proportion of Zn apportioned to the factor	factor_3[Zn]' / sum_[Zn]'	from 0,59 to 0,72	
Cl-rich	3	X	Proportion of Cl apportioned to the factor	factor_4[Cl]' /sum_[Cl]'	from 0,61 to 0,75	
Dust	4		Proportion of Ca apportioned to the factor	factor_5[Ca]'/ sum_[Ca]'	from 0,8 to 0,87	
Steel Industry	5		Proportion of Fe apportioned to the factor	factor_6[Fe]' / sum_[Fe]'	from 0,68 to 0,77	
Biomass Burning	6		Proportion of K apportioned to the factor	factor_7[K]' / sum_[K]'	from 0,54 to 0,69	
Sulfates-rich	7		Proportion of S apportioned to the factor	factor_8[S]' / sum_[S]'	from 0,74 to 0,84	
FOS						
Factor	**Criteria position**	**Constrain**	**Criterion**	**SoFi Criterion traduction**	**Static PMF Threshold Minimal proportion of tracer**	**Rolling PMF Threshold**
Shipping	0	X	Proportion of V apportioned to the factor	factor_1[V]' / sum_[V]'	from 0,68 to 0,86	Score > score of 2nd highest factor
Pb-rich	1		Proportion of Pb apportioned to the factor	factor_9[Pb]' / sum_[Pb]'	from 0,59 to 0,82	Additional threshold from 0,3 to 1

Br-related	2		Proportion of Br apportioned to the factor	factor_2[Br]' / sum_[Br]'	from 0,52 to 0,7	
Zn-industrial	3		Proportion of Zn apportioned to the factor	factor_3[Zn]' / sum_[Zn]'	from 0,57 to 0,73	
Cl-rich	4	X	Proportion of Cl apportioned to the factor	factor_4[Cl]' /sum_[Cl]'	from 0,74 to 0,85	
Dust	5		Proportion of Ca apportioned to the factor	factor_5[Ca]'/ sum_[Ca]'	from 0,81 to 0,87	
Steel Industry	6		Proportion of Fe apportioned to the factor	factor_6[Fe]' / sum_[Fe]'	from 0,63 to 0,74	
Biomass Burning	7		Proportion of K apportioned to the factor	factor_7[K]' / sum_[K]'	from 0,62 to 0,75	
Sulfates-rich	8		Proportion of S apportioned to the factor	factor_8[S]' / sum_[S]'	from 0,63 to 0,82	

Table S7: SoFi criteria used for sorting and selecting PMF runs at MRS-LCP (top) and FOS (bottom), expressed as the percentage of each major tracer element apportioned to the corresponding factor. All criteria are applied as active selection parameters, except for constrained factors (Shipping and Cl-rich), which are treated as passive criteria. The last two columns indicate the applied thresholds for factor selection in static PMF runs (YEAR, JF_D, MAM, JJA, SON) and Rolling PMF runs, respectively.

The ordering of the criteria was also important, when multiple factors shared the same elements (e.g., sulfur), necessitating prioritisation from the least abundant to the most abundant tracers. A critical step in selecting valid bootstrapped PMF runs was setting a minimum score threshold for each criterion. For each factor, the score distribution was analyzed to identify criterion score slope break points and determine suitable thresholds. All thresholds exceeded 0.5 at least, meaning that in every accepted case, the tracer element was apportioned to at least 50% in the corresponding factor. The percentage of retained bootstrapped PMF runs for each period and site is presented in Supplements, Table S8, reflecting the robustness and consistency of the seasonal PMF solutions.

	FOS	**MRS-LCP**

YEAR	49%	80%
JF_D	100%	97%
MAM	46%	83%
JJA	47%	100%
SON	28%	44%

Table S8: Percentage (%) of retained bootstrapped PMF runs for each period at both monitoring sites. Note that seasonal factors were constrained only during JJA and JF_D periods. Therefore, the percentages of retained bootstrapped PMF runs fall below 50% only for unconstrained PMF solutions.

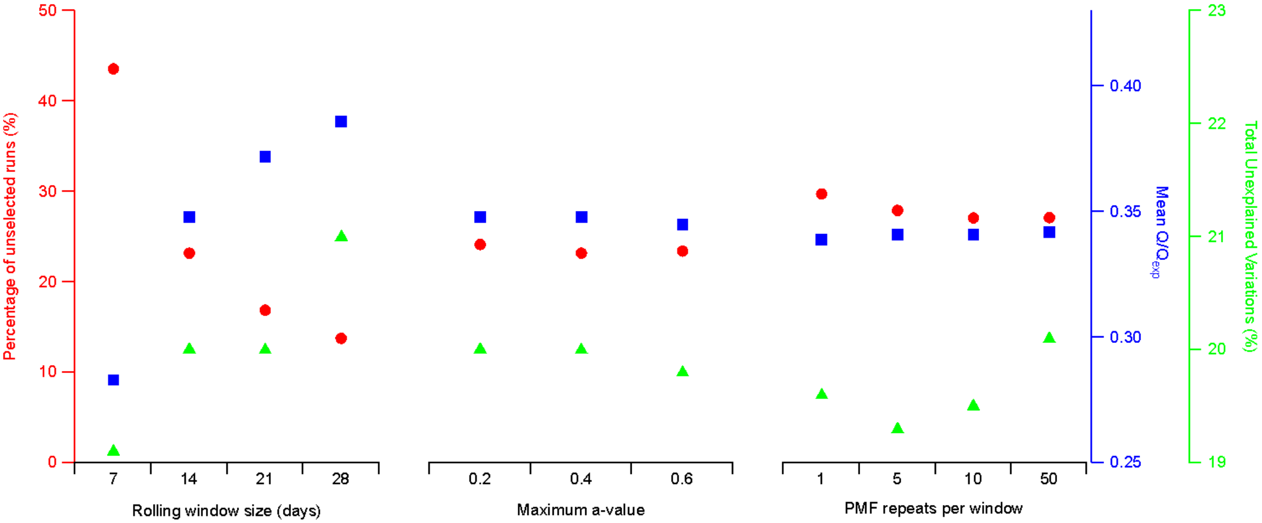

Figure S8: Statistical analysis of different rolling PMF parameters, based upon methodology developed by Canonaco et al. (2021). Statistical metrics, ie. % of selected runs (left axis, red circles), mean Q/Q$_{exp}$ (right axis, blue squares), and total unexplained variations (right axis, green triangles) over the entire dataset are reported as a function of the rolling window size (left), maximum a value with random a-value from 0 to a-value max in 0.5 (middle), and number of PMF repeats per window (right). In each plot, two of these three parameters are fixed at their optimum values and the third is varied to account for statistical variations across Rolling PMF runs. Optimum values are: rolling window size = 21 days, a-value max = 0,4 and PMF repeats per window = 50. PMF runs with varying number of PMF repeats per window (right) are bootstrapped.

PMF repeats per windows	Average amount of repeats	Minimal amount of repeats	Maximal amount of repeats
1	7	0	14

5	33	3	60
10	68	8	114
50	337	49	505

Table S9: Number of PMF repeats per modeled day for different configurations of PMF repeats per window. Each Rolling PMF analysis was performed with a maximum a-value of 0.4, incremented in 0.05 steps. The rolling window size was set to 14 days with a 1-day shift.

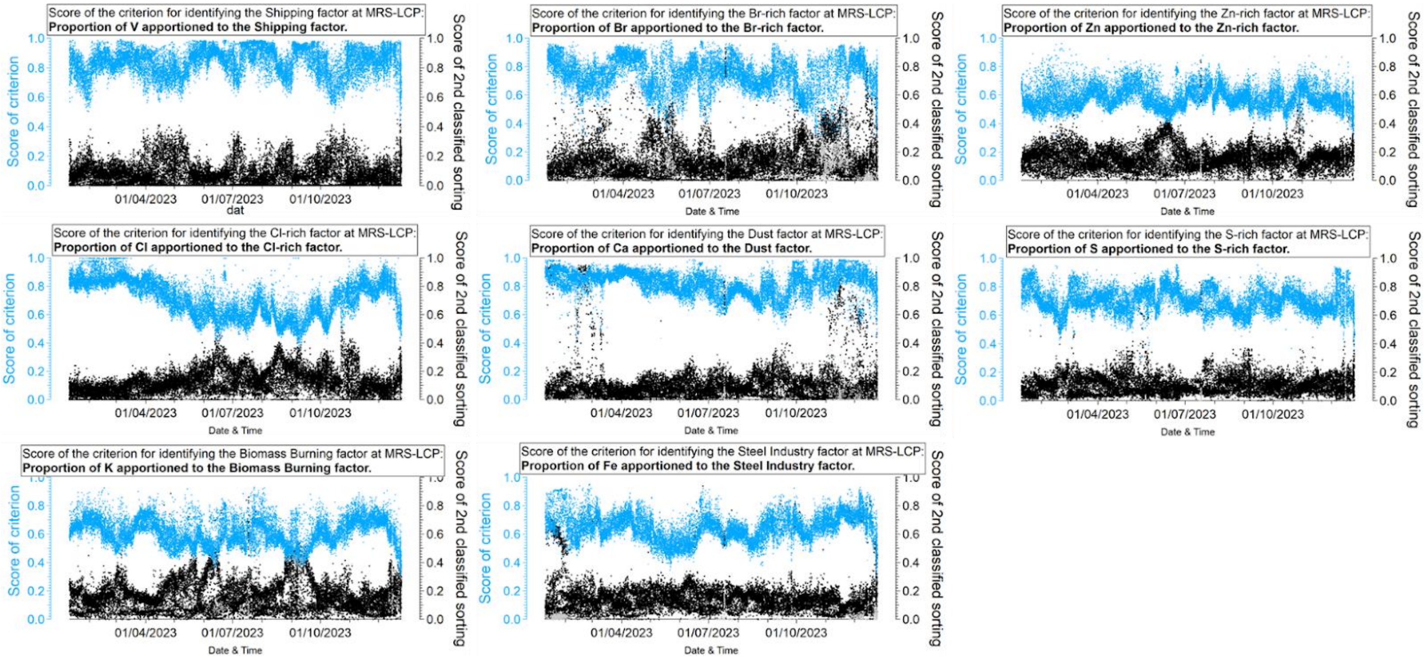

Figure S9: Rolling PMF criteria scores for the 8 PMF factors identified in MRS-LCP. Blue dots represent PMF solutions that meet the selection criteria and are included in the final PMF average. Grey dots indicate PMF runs with unsatisfactory criteria scores (i.e., lower than 0.3 or lower than the second-highest scoring factor within the same PMF solution). Black dots mark the second-highest scoring factors in each PMF solution.

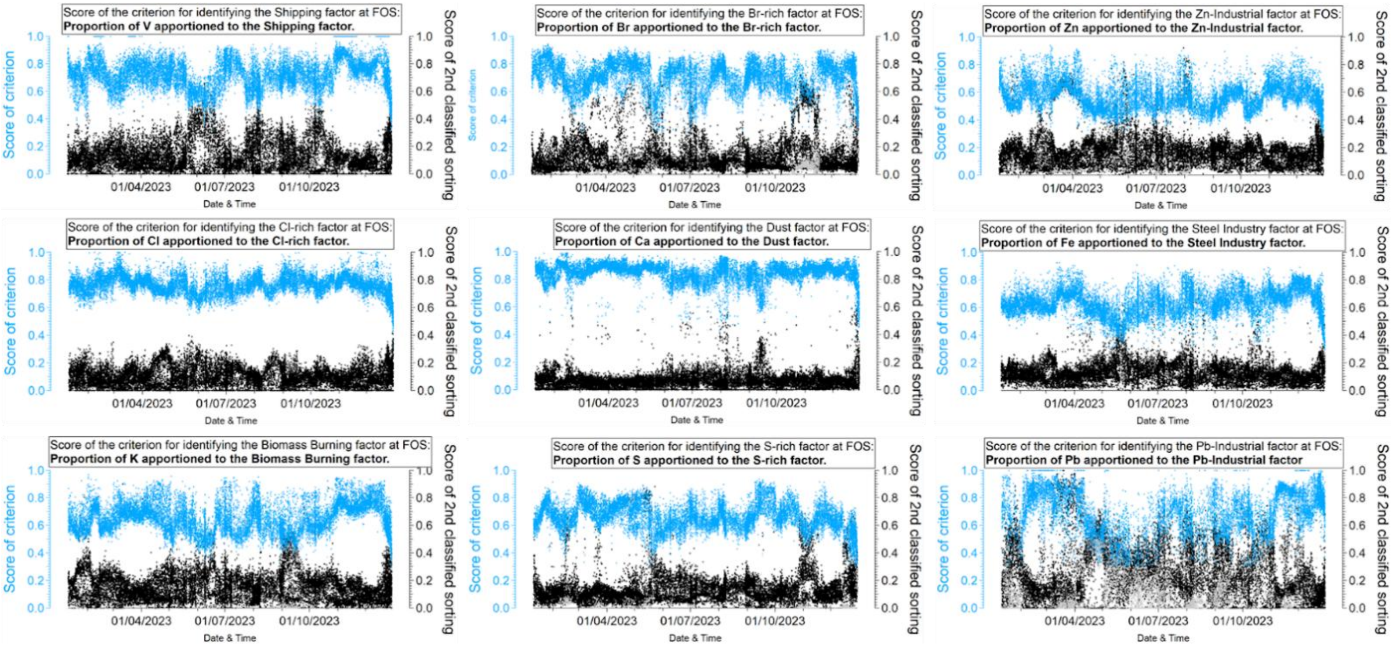

Figure S10: Rolling PMF criteria scores for the 9 PMF factors identified in FOS. Blue dots represent PMF solutions that meet the selection criteria and are included in the final PMF average. Grey dots indicate PMF runs with unsatisfactory criteria scores (i.e., lower than 0.3 or lower than the second-highest scoring factor within the same PMF solution). Black dots mark the second-highest scoring factors in each PMF solution.

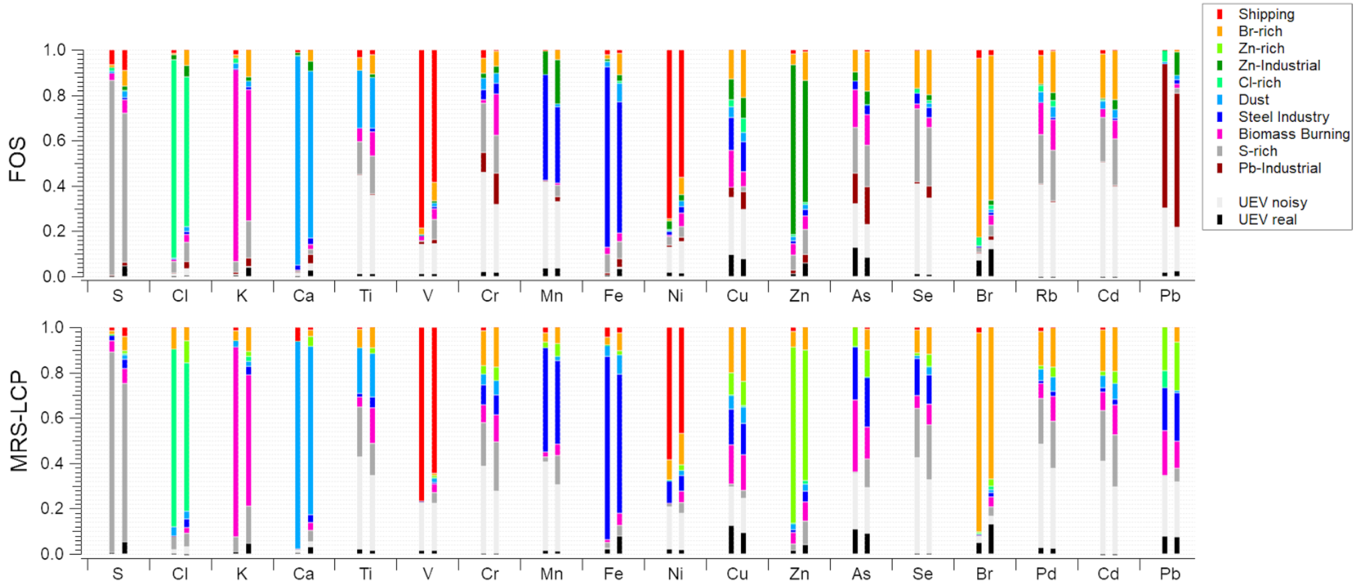

Figure S11: Explained variation for each element, for static (YEAR) PMF solution (left bars) and Rolling PMF solution (right bars), at FOS (top) and MRS-LCP (bottom).

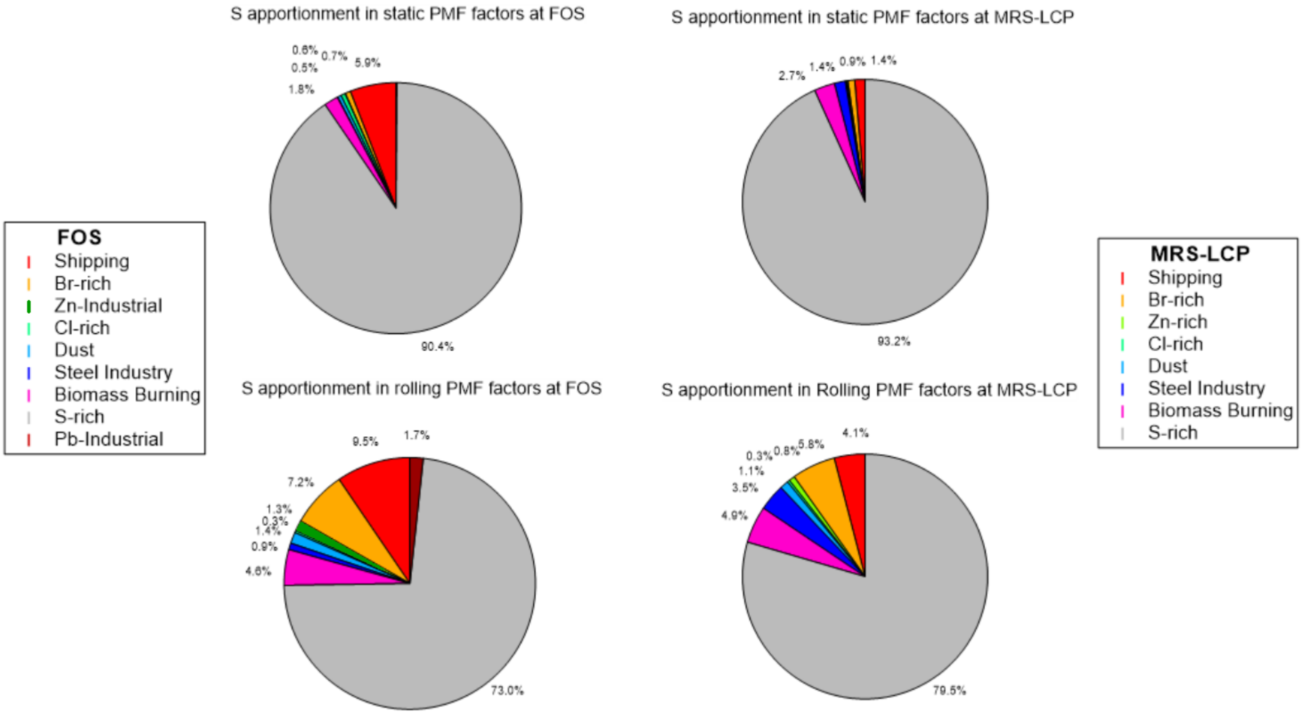

Figure S12: S apportionment in static PMF factors (top) at FOS (left) and MRS-LCP (right) versus in rolling PMF factors (bottom).

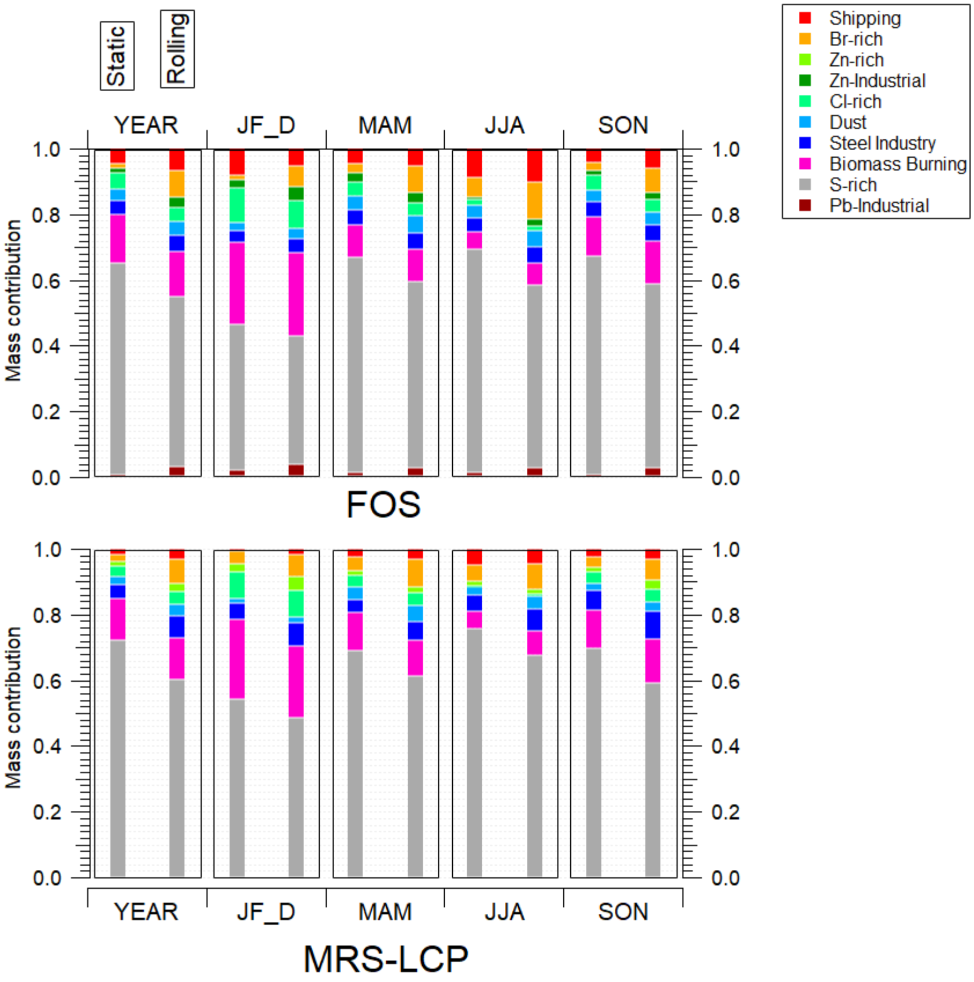

Figure S13: Factor mass contributions obtained using static (left bars) and rolling (right bars) PMF approaches, for FOS (top) and MRS-LCP (bottom), across different periods (bottom axis).

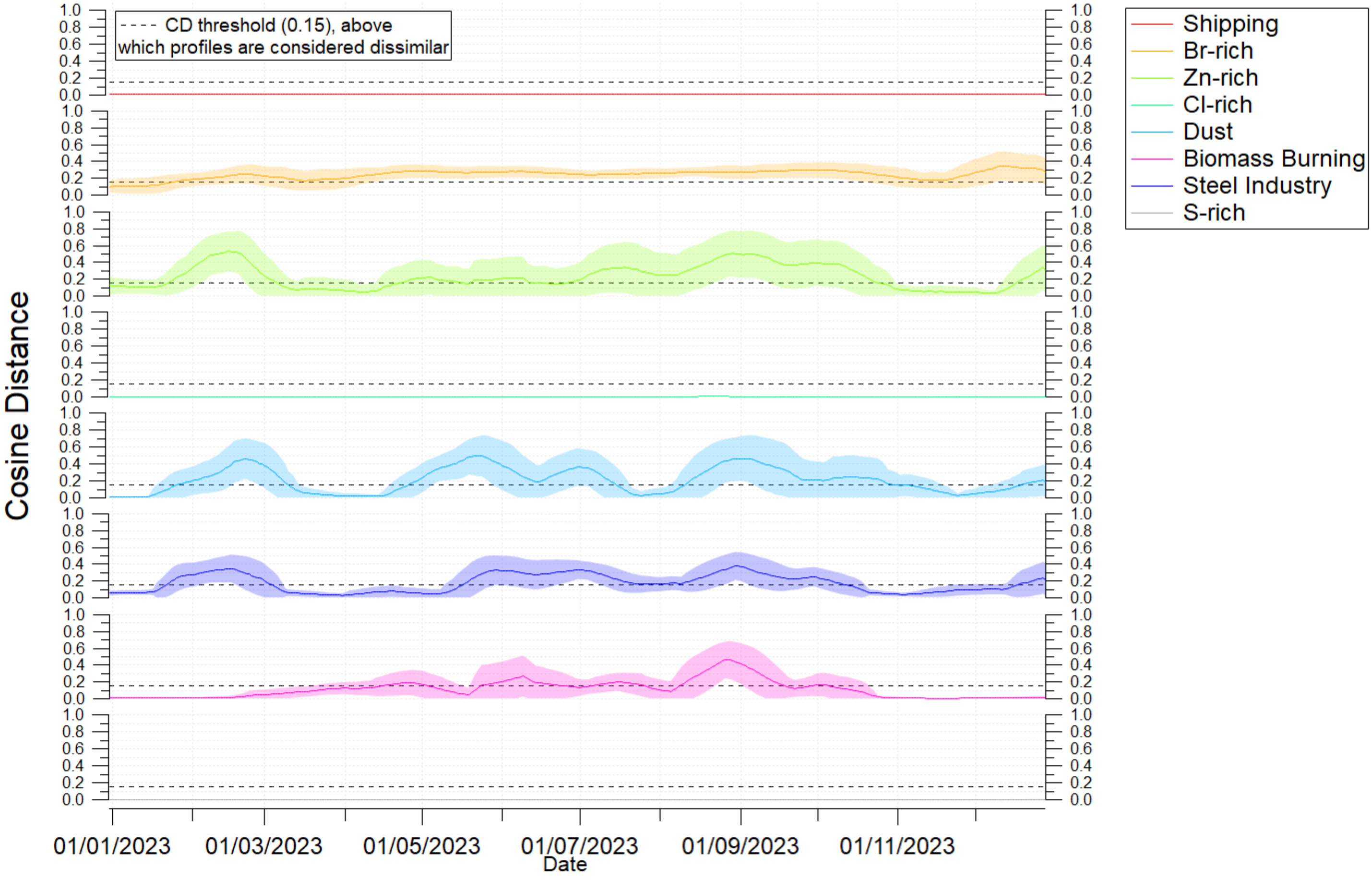

Figure S14: CD of the static (YEAR) vs. daily rolling factors for the PMF factors at MRS-LCP. Dashed lines represent threshold of dissimilarity across factors (0.15, Bougiatioti et al., 2014)

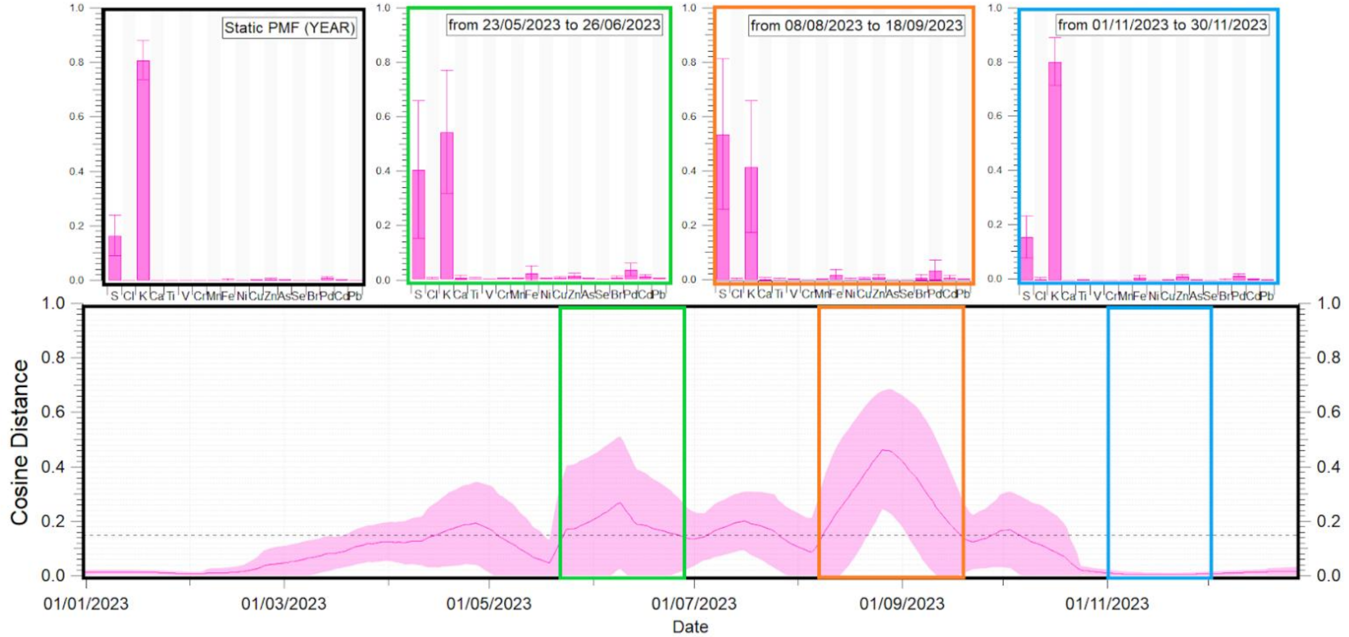

Figure S15: CD of the static (YEAR) vs. daily rolling factors and factor profiles associated to specific time of the year, for the Biomass Burning factor, at MRS-LCP. Dashed line represents threshold of dissimilarity across factors (0.15, Bougiatioti et al., 2014).

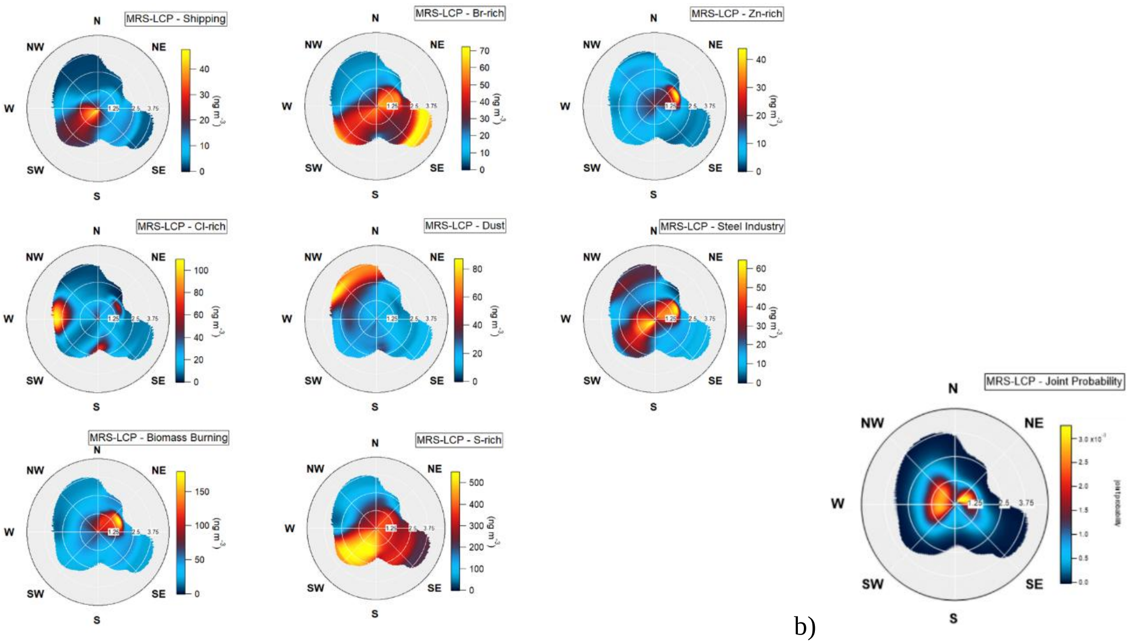

a) b)

Figure S16: a) Non-Parametric Wind Regression (NWR) showing the weighted average directional origin and associated concentrations for the 8 factors identified at MRS-LCP. NWR wind roses were calculated using the final Rolling PMF results (21-day window size, maximum a-value of 0.4, and 50 PMF repeats per window, with bootstrap enabled) over the entire measurement

campaign year. Colors indicate factor concentrations for each wind direction, while the radial axis represents wind speed for the corresponding concentrations. b) Wind Joint Probability at MRS-LCP. The radial axis represents wind speed for each occurring wind direction, while colors indicate the prevalence of the corresponding wind direction and speed.

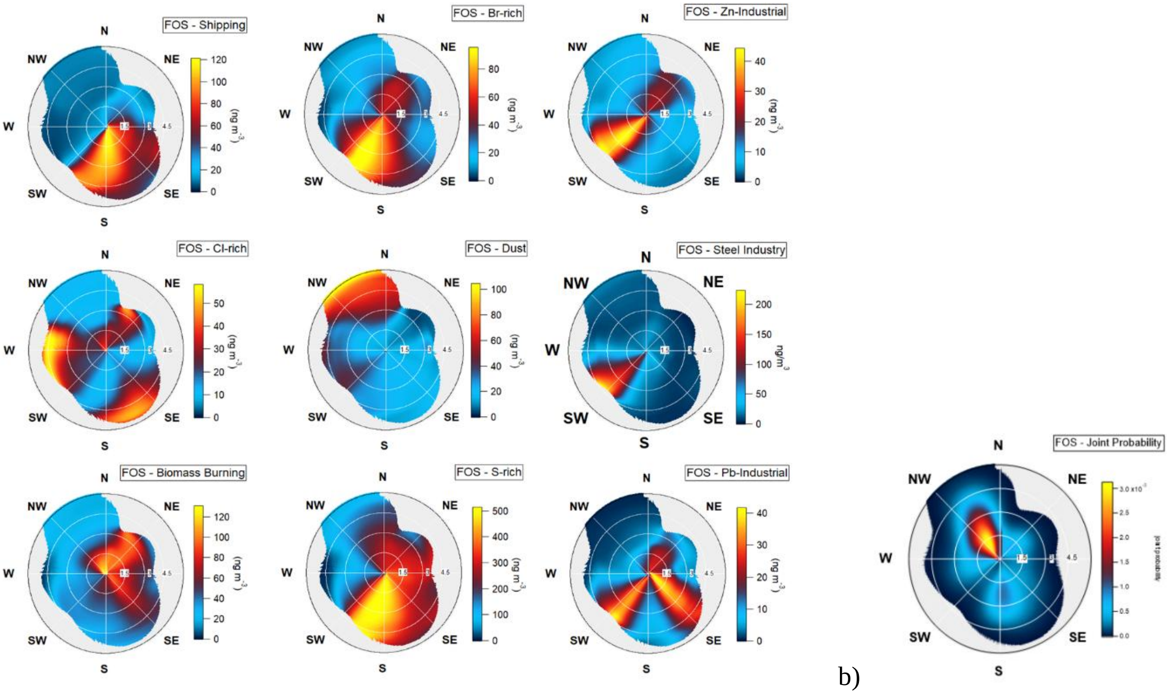

a) b)

Figure S17: a) Non-Parametric Wind Regression (NWR) showing the weighted average directional origin and associated concentrations for the 9 factors identified at FOS. NWR wind roses were calculated using the final Rolling PMF results (21-day window size, maximum a-value of 0.4, and 50 PMF repeats per window, with bootstrap enabled) over the entire measurement campaign year. Colors indicate factor concentrations for each wind direction, while the radial axis represents wind speed for the corresponding concentrations. b) Wind Joint Probability at MRS-LCP. The radial axis represents wind speed for each occurring wind direction, while colors indicate the prevalence of the corresponding wind direction and speed.

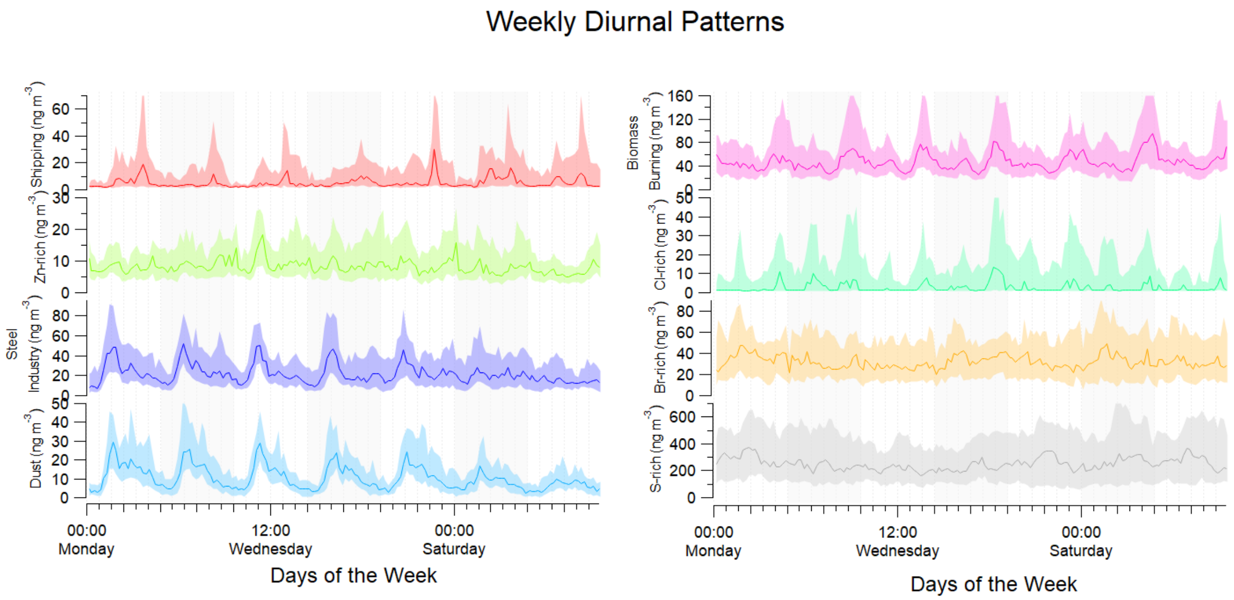

Figure S18: Weekly diurnal patterns of the rolling PMF factors at MRS-LCP. The colored lines represent the median diurnal evolution of each factor, and the light-colored areas show the interquartile range.

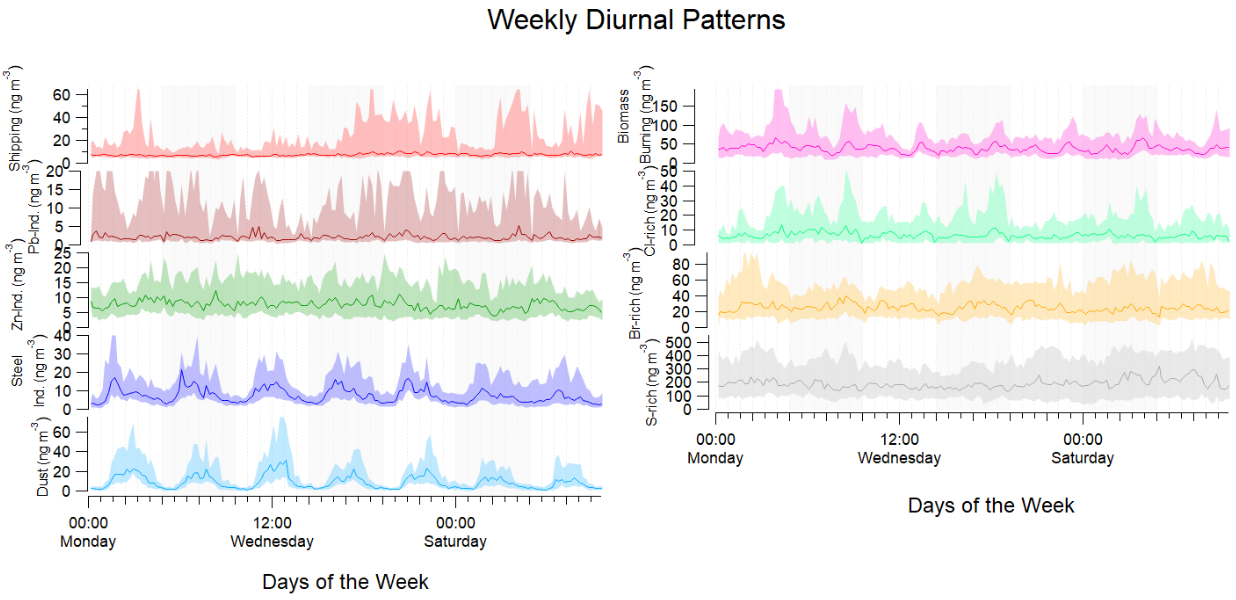

Figure S19: Weekly diurnal patterns of the rolling PMF factors at FOS. The colored lines represent the median diurnal evolution of each factor, and the light-colored areas show the interquartile range.

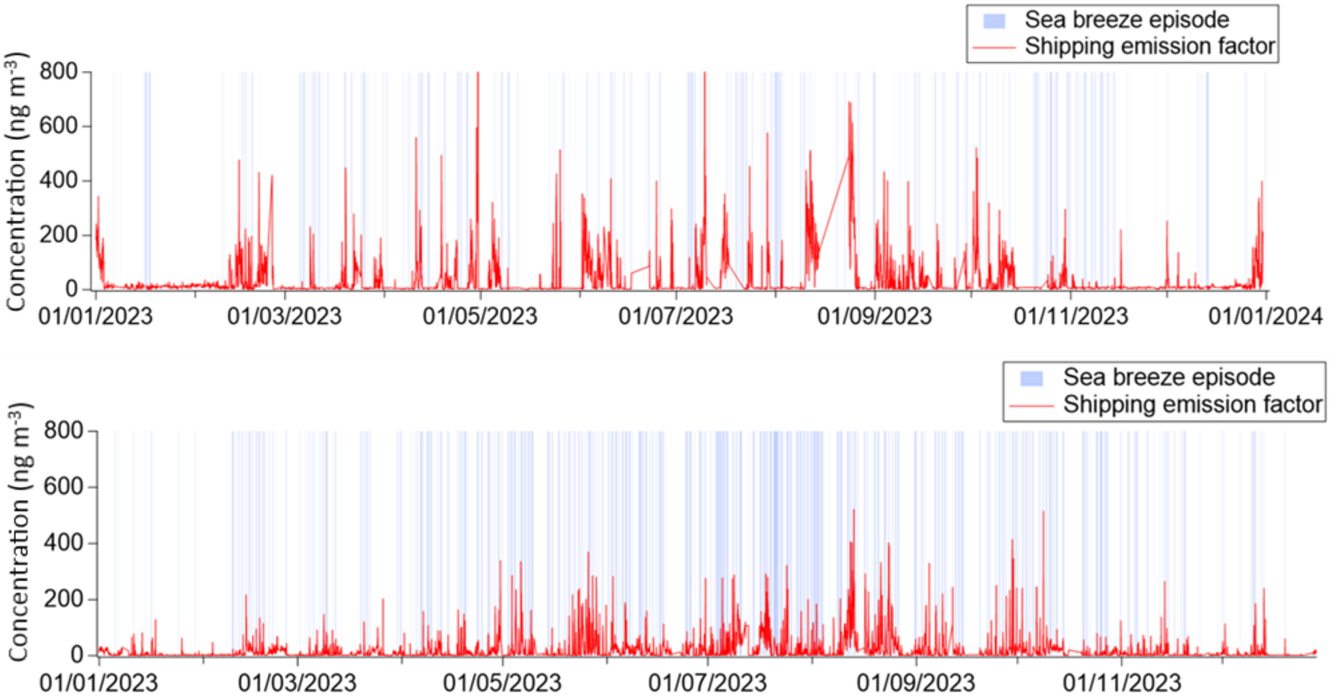

Figure S20: Shipping emission factor time series at FOS (top) and MRS-LCP (bottom) with sea breeze episodes at each station.

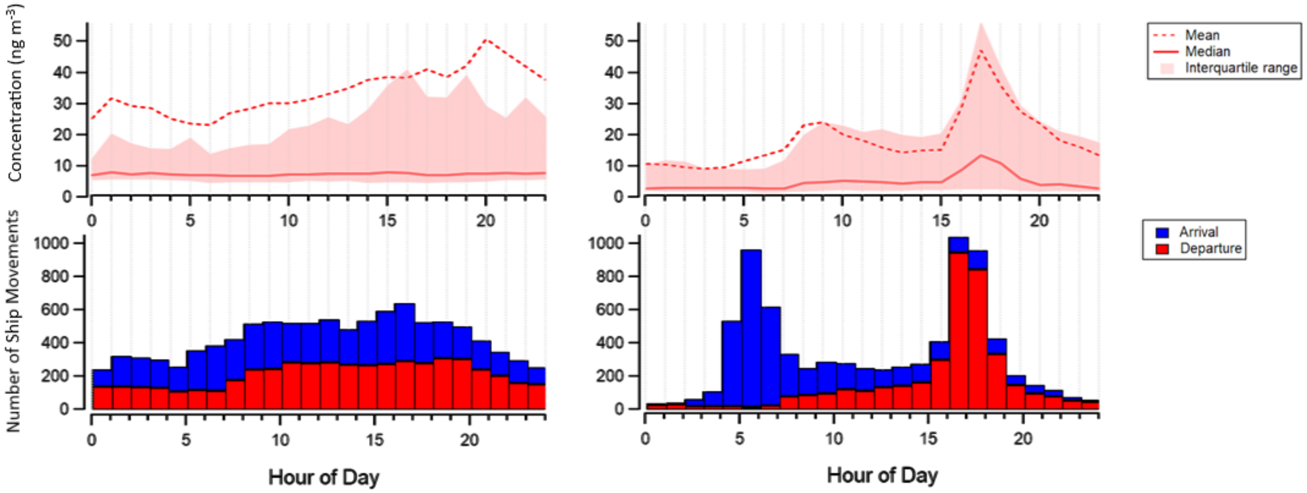

Figure S21: Diurnal profile of the Shipping factor (top) at FOS (left) and MRS-LCP (right) and cumulated number of ship movement (bottom) at Fos-sur-Mer harbour (left) and Marseille harbour (right) (GPMM).

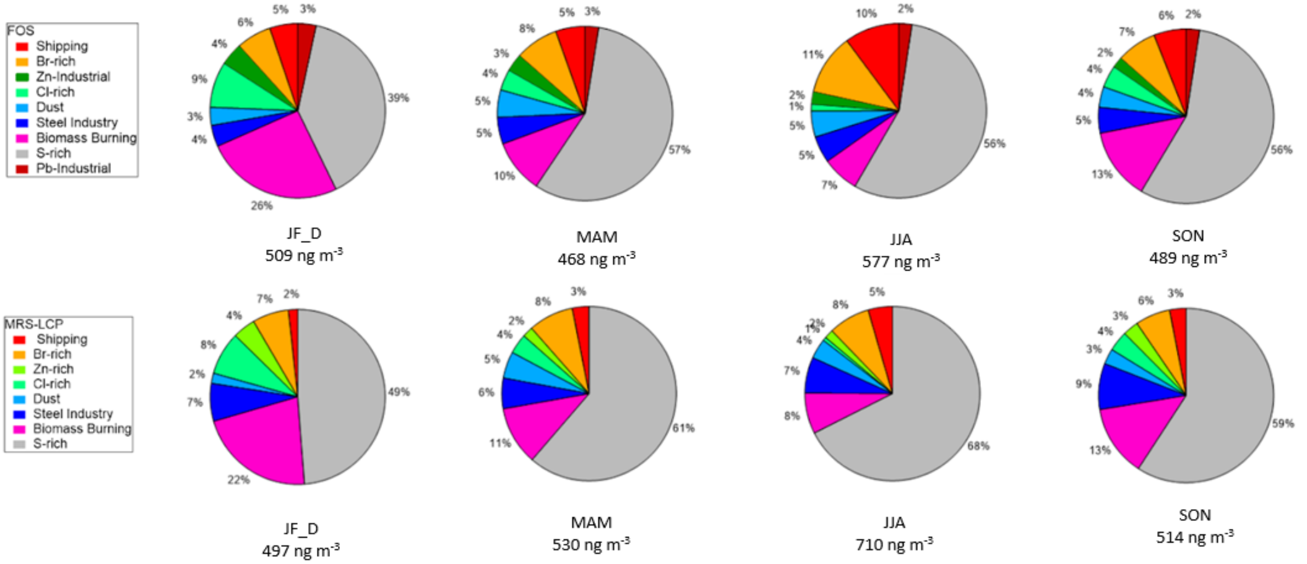

Figure S22: Pie chart showing the mass contribution of final Rolling Xact PMF factors, sliced in different seasons, for FOS (top) and MRS-LCP (bottom).

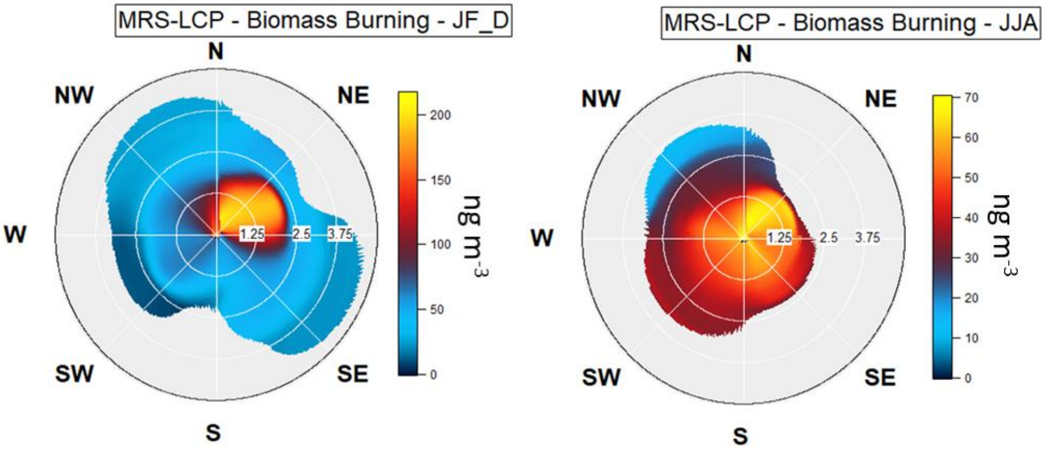

Figure S23: NWR of the Biomass Burning factor at MRS-LCP during JF_D (left) and JJA (right)

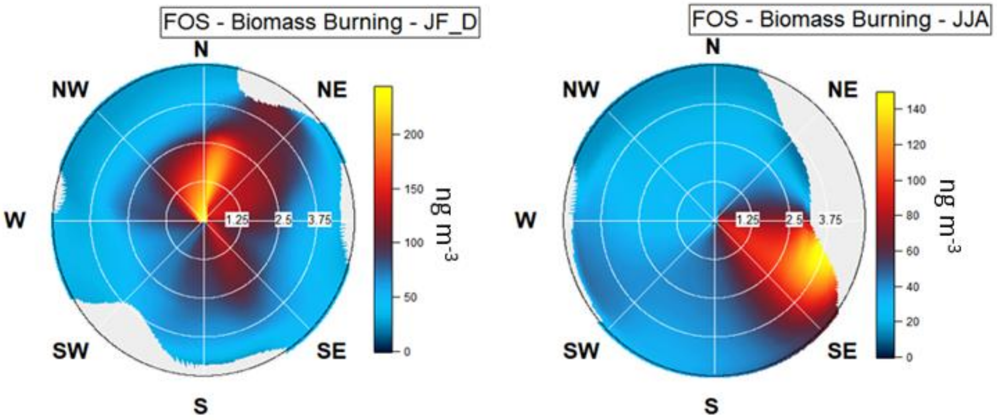

Figure S24: NWR of the Biomass Burning factor at FOS during JF_D (left) and JJA (right)

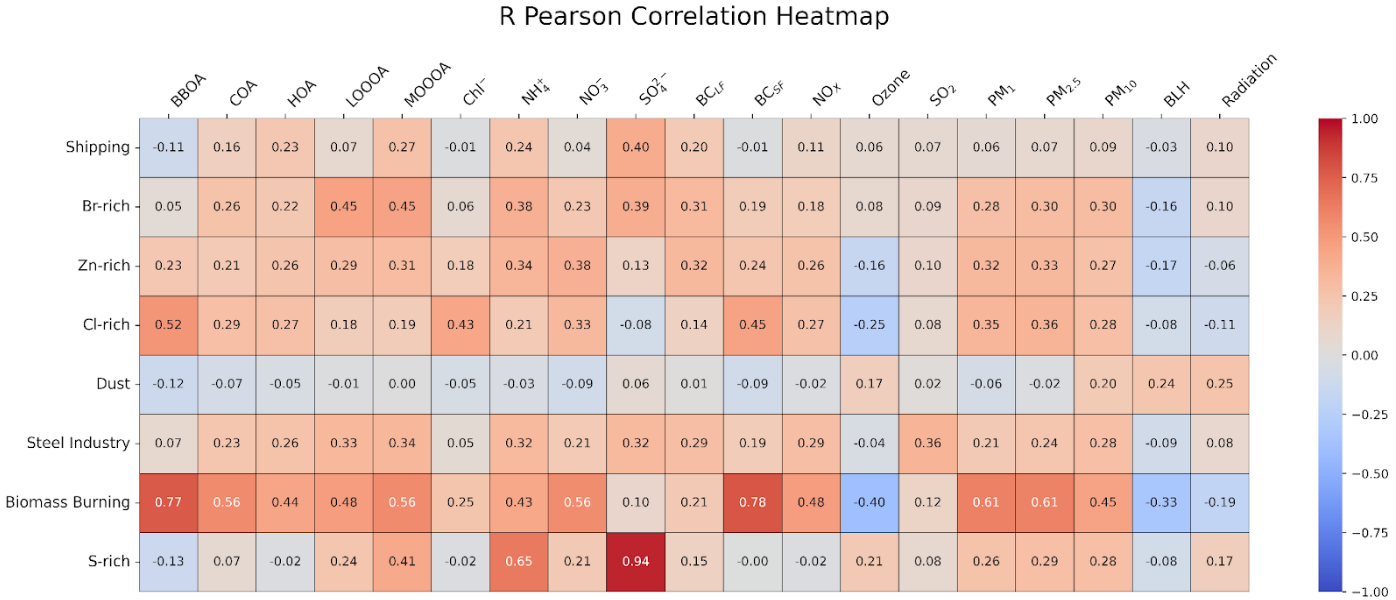

	BBOA	COA	HOA	LOOOA	MOOOA	Chl^-	NH_4^+	NO_3^-	SO_4^{2-}	BC_{LF}	BC_{SF}	NO_X	Ozone	SO_2	PM_1	$PM_{2.5}$	PM_{10}	BLH	Radiation
Shipping	-0.11	0.16	0.23	0.07	0.27	-0.01	0.24	0.04	0.40	0.20	-0.01	0.11	0.06	0.07	0.06	0.07	0.09	-0.03	0.10
Br-rich	0.05	0.26	0.22	0.45	0.45	0.06	0.38	0.23	0.39	0.31	0.19	0.18	0.08	0.09	0.28	0.30	0.30	-0.16	0.10
Zn-rich	0.23	0.21	0.26	0.29	0.31	0.18	0.34	0.38	0.13	0.32	0.24	0.26	-0.16	0.10	0.32	0.33	0.27	-0.17	-0.06
Cl-rich	0.52	0.29	0.27	0.18	0.19	0.43	0.21	0.33	-0.08	0.14	0.45	0.27	-0.25	0.08	0.35	0.36	0.28	-0.08	-0.11
Dust	-0.12	-0.07	-0.05	-0.01	0.00	-0.05	-0.03	-0.09	0.06	0.01	-0.09	-0.02	0.17	0.02	-0.06	-0.02	0.20	0.24	0.25
Steel Industry	0.07	0.23	0.26	0.33	0.34	0.05	0.32	0.21	0.32	0.29	0.19	0.29	-0.04	0.36	0.21	0.24	0.28	-0.09	0.08
Biomass Burning	0.77	0.56	0.44	0.48	0.56	0.25	0.43	0.56	0.10	0.21	0.78	0.48	-0.40	0.12	0.61	0.61	0.45	-0.33	-0.19
S-rich	-0.13	0.07	-0.02	0.24	0.41	-0.02	0.65	0.21	0.94	0.15	-0.00	-0.02	0.21	0.08	0.26	0.29	0.28	-0.08	0.17

Figure S25: Heatmap of $R_{Pearson}$ correlation coefficient for Rolling PMF factors vs. external data (ToF-ACSM SIA and Rolling PMF OA, BC_{SF} and BC_{LF} from AE33, NO_X, Ozone, SO_2, PM_1, $PM_{2.5}$, PM_{10} from FIDAS, BLH and shortwave radiation from Open-Meteo) at MRS-LCP.

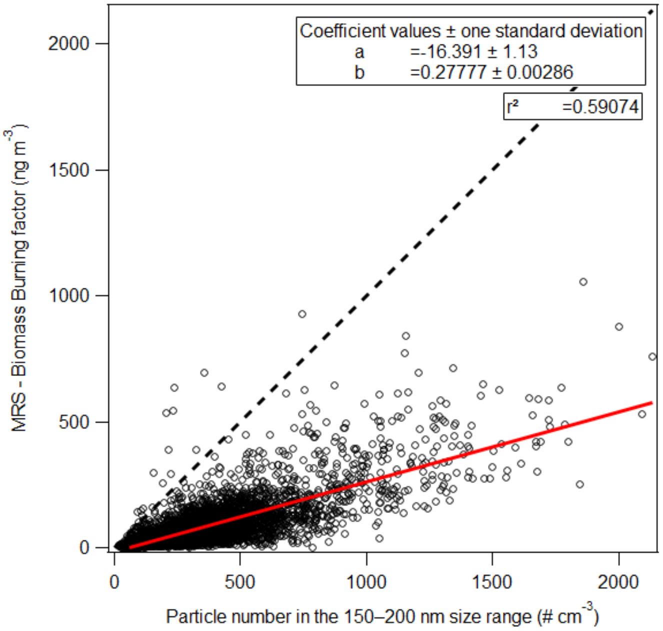

Figure S26: Linear correlation between Xact Biomass Burning factor and particle number in the 150-200 nm size range, at MRS-LCP

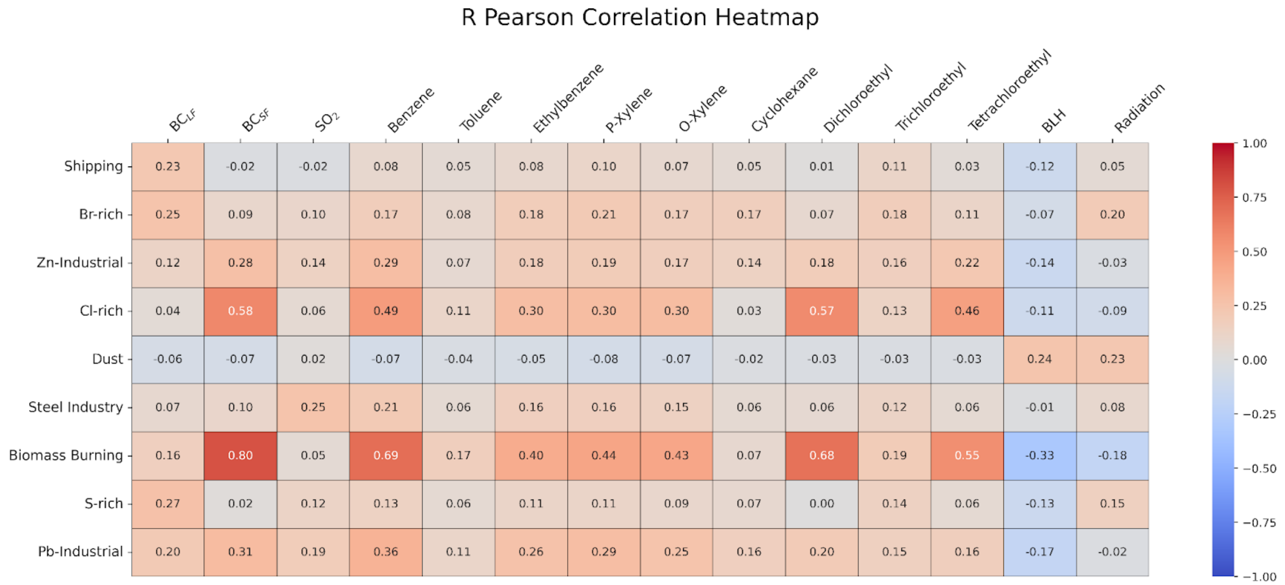

	BC_{LF}	BC_{SF}	SO_2	Benzene	Toluene	Ethylbenzene	P-Xylene	O-Xylene	Cyclohexane	Dichloroethyl	Trichloroethyl	Tetrachloroethyl	BLH	Radiation
Shipping	0.23	-0.02	-0.02	0.08	0.05	0.08	0.10	0.07	0.05	0.01	0.11	0.03	-0.12	0.05
Br-rich	0.25	0.09	0.10	0.17	0.08	0.18	0.21	0.17	0.17	0.07	0.18	0.11	-0.07	0.20
Zn-Industrial	0.12	0.28	0.14	0.29	0.07	0.18	0.19	0.17	0.14	0.18	0.16	0.22	-0.14	-0.03
Cl-rich	0.04	0.58	0.06	0.49	0.11	0.30	0.30	0.30	0.03	0.57	0.13	0.46	-0.11	-0.09
Dust	-0.06	-0.07	0.02	-0.07	-0.04	-0.05	-0.08	-0.07	-0.02	-0.03	-0.03	-0.03	0.24	0.23
Steel Industry	0.07	0.10	0.25	0.21	0.06	0.16	0.16	0.15	0.06	0.06	0.12	0.06	-0.01	0.08
Biomass Burning	0.16	0.80	0.05	0.69	0.17	0.40	0.44	0.43	0.07	0.68	0.19	0.55	-0.33	-0.18
S-rich	0.27	0.02	0.12	0.13	0.06	0.11	0.11	0.09	0.07	0.00	0.14	0.06	-0.13	0.15
Pb-Industrial	0.20	0.31	0.19	0.36	0.11	0.26	0.29	0.25	0.16	0.20	0.15	0.16	-0.17	-0.02

Figure S27: Heatmap of $R_{Pearson}$ correlation coefficient for Rolling PMF factors vs. external data (BC_{SF} and BC_{LF} from AE33, SO_2, VOCs, BLH and shortwave radiation from Open-Meteo) at FOS.

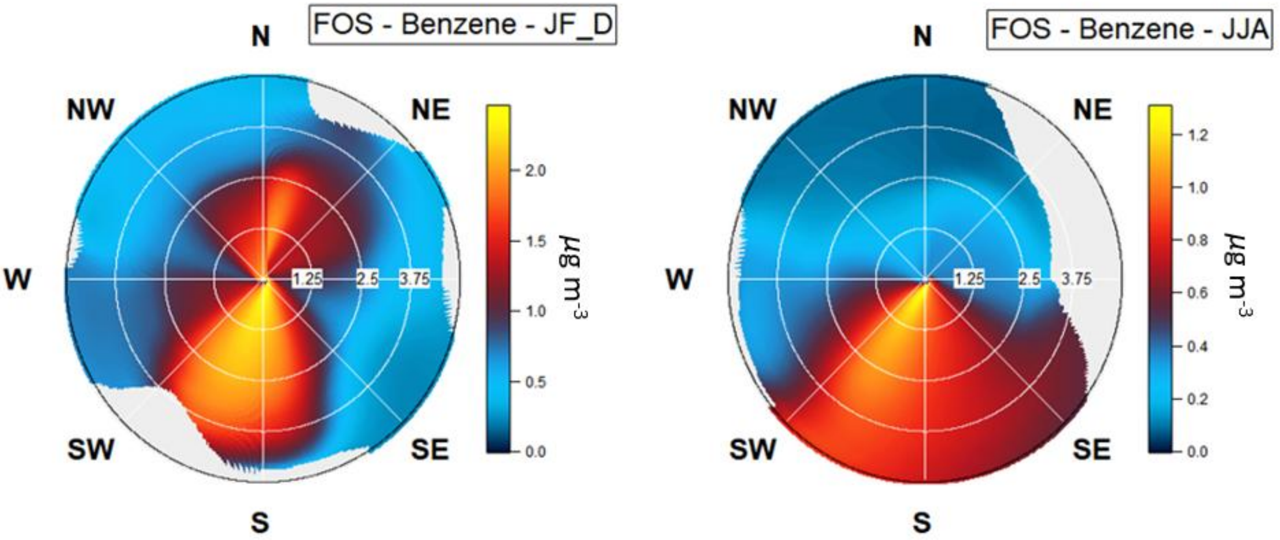

Figure S28: NWR of the Benzene at FOS during JF_D (left) and JJA (right)

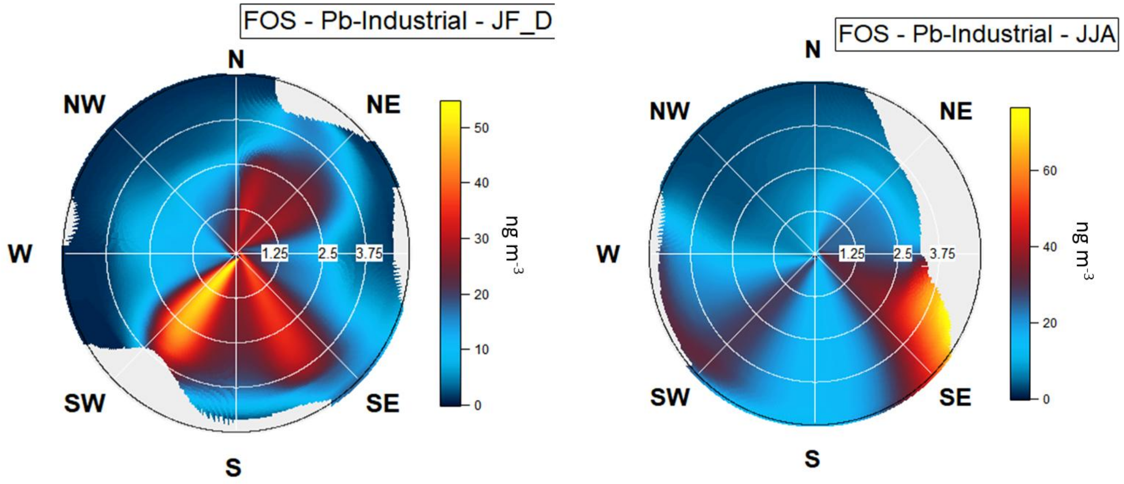

Figure S29: NWR of the Pb-Industrial factor at FOS during JF_D (left) and JJA (right)

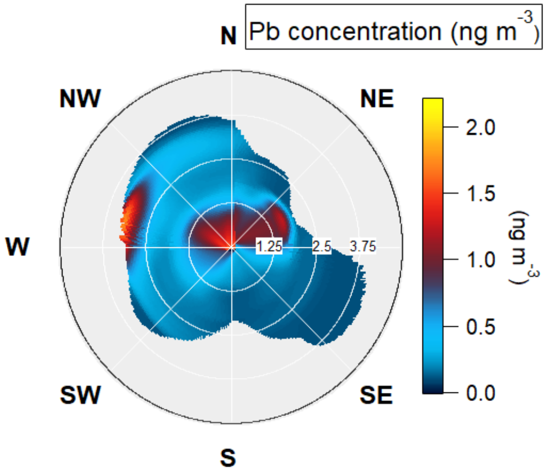

Figure S30: NWR of the Pb element at MRS-LCP.

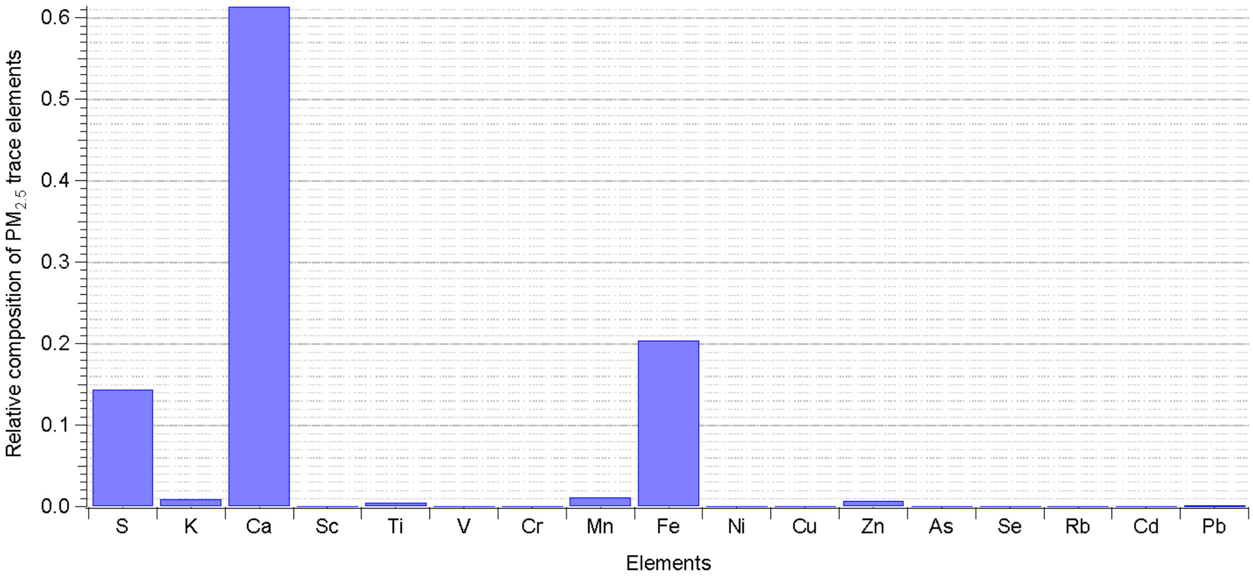

Figure S31: Relative composition of $PM_{2.5}$ trace elements for the 4 treatment units in the steel industry complex of Fos-sur-Mer, adapted from Sylvestre et al., 2017. Filters were collected at various locations downwind of the treatment units. Trace elements and major ions (SO_4^{2-}, NO_3^-, NH_4^+, Na^+, K^+, Mg^{2+} and Ca^{2+}) were analyzed using ion chromatography. Elemental sulfur contribution was estimated using the molar mass ratio of sulfate to sulfur of (3:1).

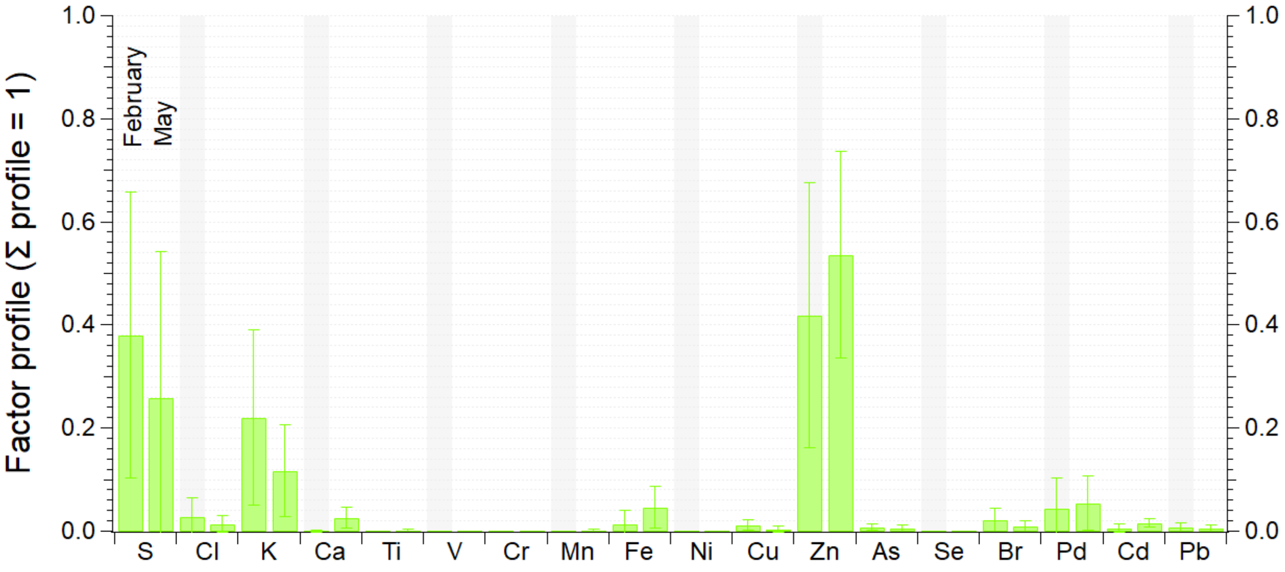

Figure S32: Zn-rich factor composition at different times of the year (February, left bars; May, right bars) at MRS-LCP. Colored bars represent the average rolling factor composition for each month, and error bars indicate the standard deviation.

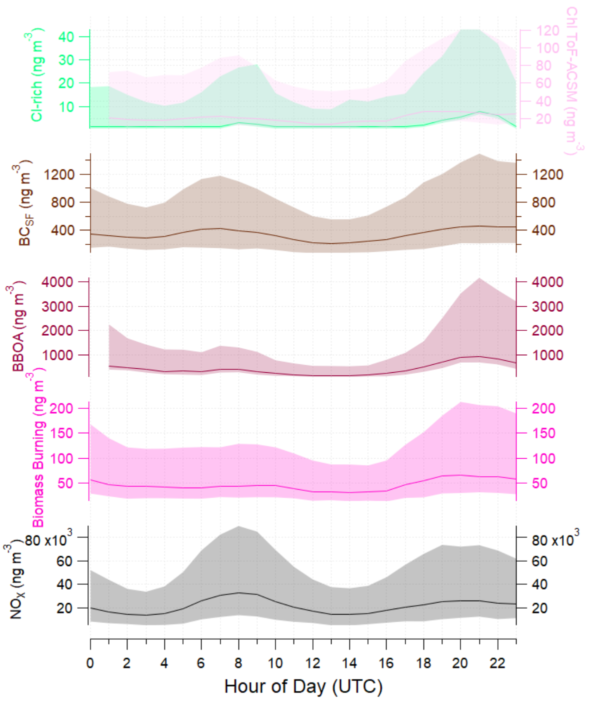

Figure S33: Median diurnal cycles for BBOA, BC$_{SF}$, NO$_X$, Biomass Burning and Cl-rich Xact Rolling PMF factors at MRS-LCP. The light-colored areas show the interquartile range.

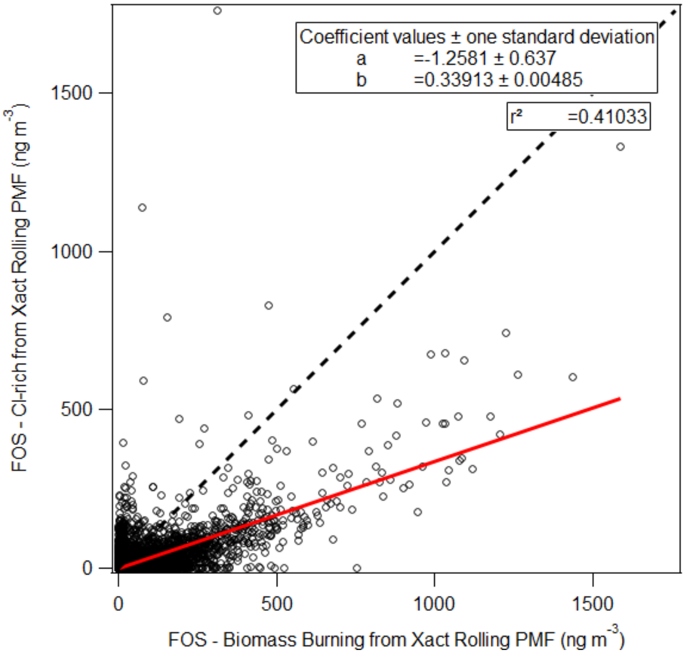

Figure S34: Linear correlation between Xact Biomass Burning and Cl-rich factors at FOS

S6: Sea Salt Dechlorination

Another potential source of particulate chlorine is sea salt dechlorination (Jordan et al., 2015), however it was not considered dominant in this case for the following reasons: a) Particle size: Sea salt is primarily emitted in the coarse fraction, while chlorine formation via acid displacement is more efficient in fine particles (Faxon & Allen, 2013). b) Seasonality: The Cl-rich factor peaked in winter, when thermal breezes that could transport marine aerosols are less frequent. c) Isotopic ratio (Fig. S35): to test for a sea salt origin, the Na^{35}/Na^{37} ratio was examined using the m/z 58 / m/z 60 ratio in ToF-ACSM data at MRS-LCP. The typical sea salt ratio is ~3.1 (De Laeter et al., 2003), but values at MRS-LCP were generally lower (median: 1.63), particularly in winter (~0.8), likely due to levoglucosan interference at m/z 60. d) NWR analysis: No dominant marine origin was observed, the factor had varied source directions, an few consistent with sea salt. e) Sea-salt aerosol is not expected to be a dominant contributor in the Mediterranean environment, as reduced wave breaking limits sea-salt emission. f) Weak correlation is observed between the chlorine signals from the ToF-ACSM and the Xact at MRS-LCP ($R^2 = 0.44$, Fig. S36). Previous studies also indicate that this poor correlation might be related to the lack of chlorine calibration on the MRS-LCP ToF-ACSM, and to the mostly refractory nature of NaCl, who tends to tends to bounce off the ToF-ACSM's vaporizer, without capture system (Ovadnevaite et al., 2012; Tobler et al., 2020; Sustrena et al., 2024). Finally, a slight overestimation of chlorine by the ToF-ACSM compared to Xact is observed (Fig. S36), which suggests substantial errors in chlorine estimation by the ACSM (Tobler et al., 2020), possibly due to organochloride misclassification (Wang and Ruiz, 2017).

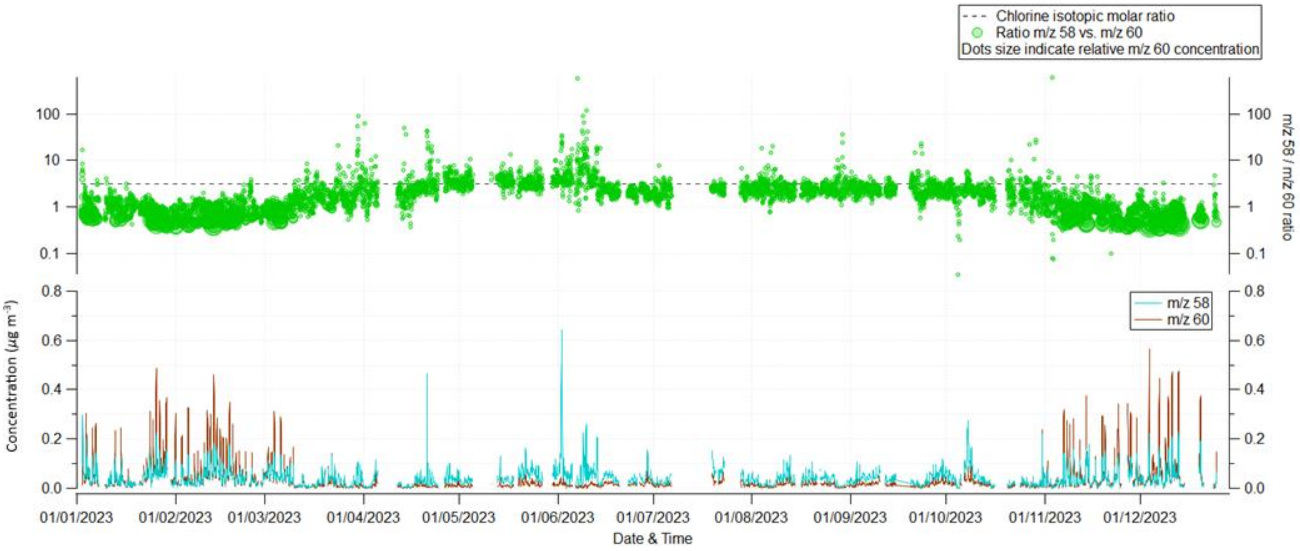

Figure S35: Time series of m/z 58 and m/z 60 from the ToF-ACSM at the MRS-LCP station over the year 2023 (bottom) and ratio of the 2 fragments compared to the chlorine isotopic molar ratio (top).

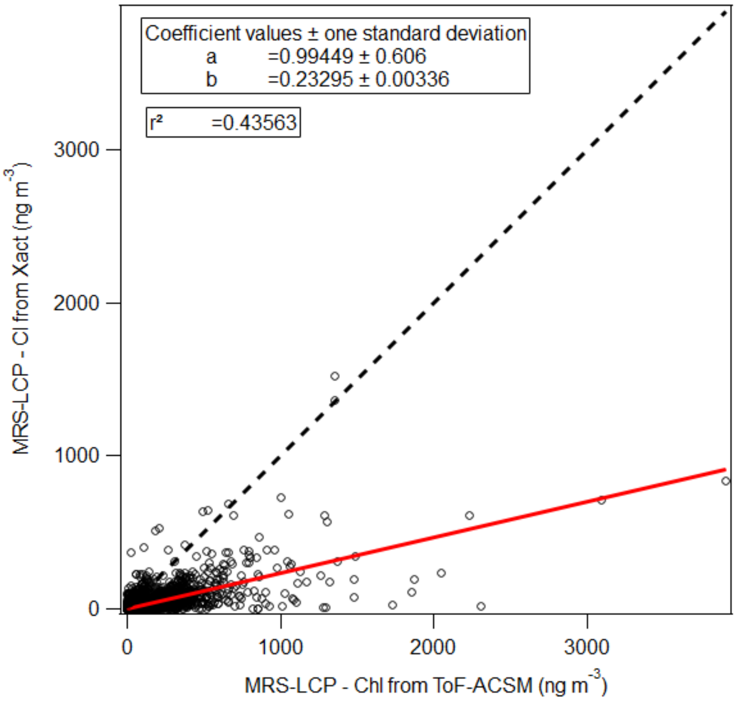

Figure S36: Linear correlation of the Cl from Xact and the Chl from ToF-ACSM at MRS-LCP, 2023.

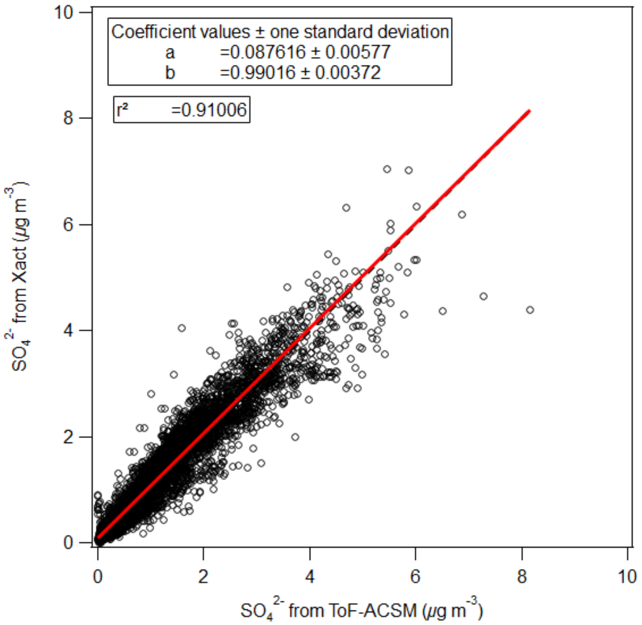

Figure S37: Linear correlation between sulfate mass reconstructed from the elemental S (Xact) and sulfate concentrations measured by ACSM, for MRS-LCP. The sulfate mass from the elemental S is estimated by applying a multiplication factor of 3, corresponding to the molar mass ratio of sulfate to elemental sulfur (Furger et al., 2017).

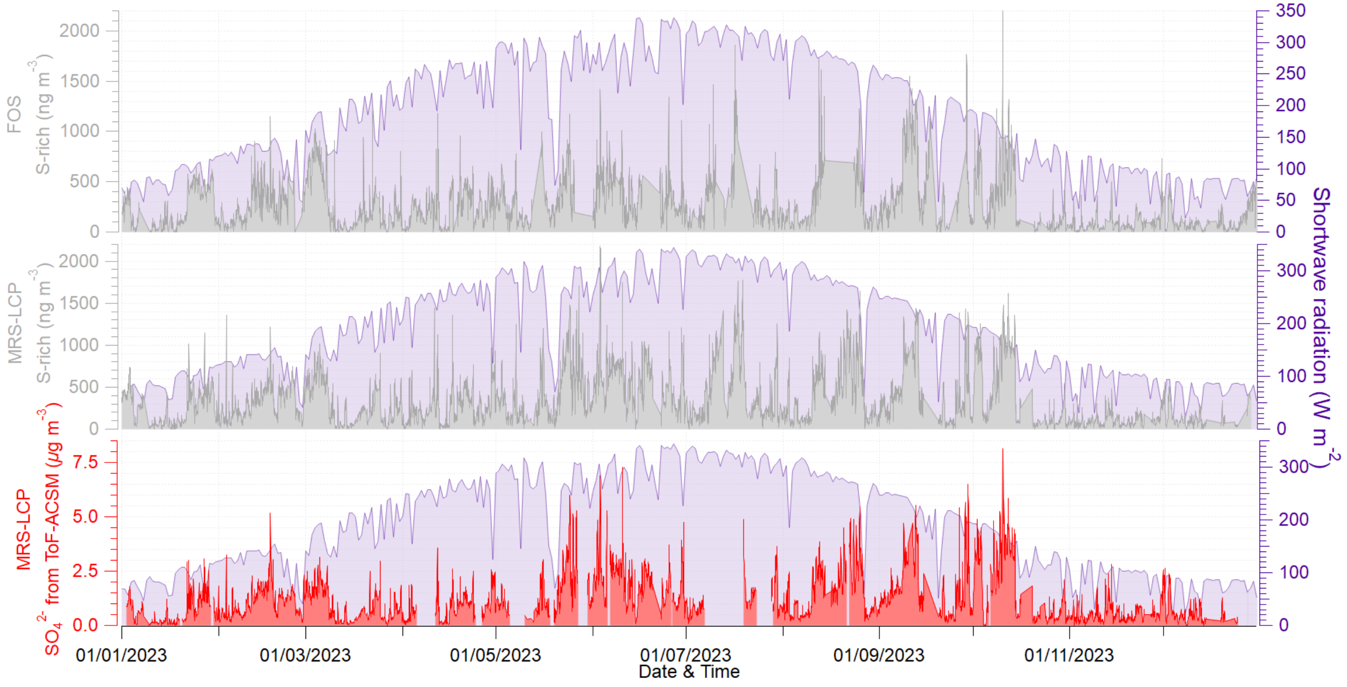

Figure S38: Time series of S-rich factor concentrations and shortwave radiation at FOS (top) and MRS-LCP (bottom), respectively, and SO_4^{2-} from ToF-ACSM (MRS-LCP).

References

Belis, C. A., Pernigotti, D., Karagulian, F., Pirovano, G., Larsen, B. R., Gerboles, M., and Hopke, P. K.: A new methodology to assess the performance and uncertainty of source apportionment models in intercomparison exercises, Atmospheric Environment, 119, 35–44, https://doi.org/10.1016/j.atmosenv.2015.08.002, 2015.

Belis, C. A., Pikridas, M., Lucarelli, F., Petralia, E., Cavalli, F., Calzolai, G., Berico, M., and Sciare, J.: Source apportionment of fine PM by combining high time resolution organic and inorganic chemical composition datasets, Atmospheric Environment: X, 3, 100046, https://doi.org/10.1016/j.aeaoa.2019.100046, 2019.

Bougiatioti, A., Stavroulas, I., Kostenidou, E., Zarmpas, P., Theodosi, C., Kouvarakis, G., Canonaco, F., Prévôt, A. S. H., Nenes, A., Pandis, S. N., and Mihalopoulos, N.: Processing of biomass-burning aerosol in the eastern Mediterranean during summertime, Atmos. Chem. Phys., 14, 4793–4807, https://doi.org/10.5194/acp-14-4793-2014, 2014.

Brown, S. G., Eberly, S., Paatero, P., and Norris, G. A.: Methods for estimating uncertainty in PMF solutions: Examples with ambient air and water quality data and guidance on reporting PMF results, Science of The Total Environment, 518–519, 626–635, https://doi.org/10.1016/j.scitotenv.2015.01.022, 2015.

Camman, J., Chazeau, B., Marchand, N., Durand, A., Gille, G., Lanzi, L., Jaffrezo, J.-L., Wortham, H., and Uzu, G.: Oxidative potential apportionment of atmospheric PM_1 : A new approach combining high-sensitive online analysers for chemical composition and offline OP measurement technique, https://doi.org/10.5194/egusphere-2023-1441, 2024.

Canonaco, F., Tobler, A., Chen, G., Sosedova, Y., Slowik, J. G., Bozzetti, C., Daellenbach, K. R., El Haddad, I., Crippa, M., Huang, R.-J., Furger, M., Baltensperger, U., and Prévôt, A. S. H.: A new method for long-term source apportionment with time-dependent factor profiles and uncertainty assessment using SoFi Pro: application to 1 year of organic aerosol data, Atmos. Meas. Tech., 14, 923–943, https://doi.org/10.5194/amt-14-923-2021, 2021.

Efron, B. "Bootstrap Methods: Another Look at the Jackknife." The Annals of Statistics, vol. 7, no. 1, pp. 1–26. JSTOR, http://www.jstor.org/stable/2958830, 1979.

Faxon, C. B. and Allen, D. T.: Chlorine chemistry in urban atmospheres: a review, Environ. Chem., 10, 221, https://doi.org/10.1071/EN13026, 2013.

De Laeter, J. R., Böhlke, J. K., De Bièvre, P., Hidaka, H., Peiser, H. S., Rosman, K. J. R., and Taylor, P. D. P.: Atomic weights of the elements: Review 2000 (IUPAC Technical Report), Pure Appl. Chem., 75, 683–800, 2003.

Fossum, K. N., Lin, C., O'Sullivan, N., Lei, L., Hellebust, S., Ceburnis, D., Afzal, A., Tremper, A., Green, D., Jain, S., Byčenkienė, S., O'Dowd, C., Wenger, J., and Ovadnevaite, J.: Two distinct ship emission profiles for organic-sulfate source apportionment of PM in sulfur emission control areas, Atmos. Chem. Phys., 24, 10815–10831, https://doi.org/10.5194/acp-24-10815-2024, 2024.

Furger, M., Minguillón, M. C., Yadav, V., Slowik, J. G., Hüglin, C., Fröhlich, R., Petterson, K., Baltensperger, U., and Prévôt, A. S. H.: Elemental composition of ambient aerosols measured with high temporal resolution using an online XRF spectrometer, Atmos. Meas. Tech., 10, 2061–2076, https://doi.org/10.5194/amt-10-2061-2017, 2017.

Heutte, B.: Measurements of aerosol microphysical and chemical properties in the central Arctic atmosphere during MOSAiC, n.d.

Hopke, P. K., Dai, Q., Li, L., and Feng, Y.: Global review of recent source apportionments for airborne particulate matter, Science of The Total Environment, 740, 140091, https://doi.org/10.1016/j.scitotenv.2020.140091, 2020.

Jordan, C. E., Pszenny, A. A. P., Keene, W. C., Cooper, O. R., Deegan, B., Maben, J., Routhier, M., Sander, R., and Young, A. H.: Origins of aerosol chlorine during winter over north central Colorado, USA, JGR Atmospheres, 120, 678–694, https://doi.org/10.1002/2014JD022294, 2015.

Manigrasso, M., Soggiu, M. E., Settimo, G., Inglessis, M., Protano, C., Vitali, M., and Avino, P.: PM Dimensional Characterization in an Urban Mediterranean Area: Case Studies on the Separation between Fine and Coarse Atmospheric Aerosol, Atmosphere, 13, 227, https://doi.org/10.3390/atmos13020227, 2022.

Manousakas, M., Furger, M., Daellenbach, K. R., Canonaco, F., Chen, G., Tobler, A., Rai, P., Qi, L., Tremper, A. H., Green, D., Hueglin, C., Slowik, J. G., El Haddad, I., and Prevot, A. S. H.: Source identification of the elemental fraction of particulate matter using size segregated, highly time-resolved data and an optimized source apportionment approach, Atmospheric Environment: X, 14, 100165, https://doi.org/10.1016/j.aeaoa.2022.100165, 2022.

Ovadnevaite, J., Ceburnis, D., Canagaratna, M., Berresheim, H., Bialek, J., Martucci, G., Worsnop, D. R., and O'Dowd, C.: On the effect of wind speed on submicron sea salt mass concentrations and source fluxes, J. Geophys. Res., 117, 2011JD017379, https://doi.org/10.1029/2011JD017379, 2012.

Paatero, P.: The Multilinear Engine: A Table-Driven, Least Squares Program for Solving Multilinear Problems, including the n-Way Parallel Factor Analysis Model, 2024.

Paatero, P., Hopke, P. K., Song, X.-H., and Ramadan, Z.: Understanding and controlling rotations in factor analytic models, Chemometrics and Intelligent Laboratory Systems, 60, 253–264, https://doi.org/10.1016/S0169-7439(01)00200-3, 2002.

Pernigotti, D. and Belis, C. A.: DeltaSA tool for source apportionment benchmarking, description and sensitivity analysis, Atmospheric Environment, 180, 138–148, https://doi.org/10.1016/j.atmosenv.2018.02.046, 2018.

Paatero, P. and Hopke, P. K.: Discarding or downweighting high-noise variables in factor analytic models, Analytica Chimica Acta, 490, 277–289, https://doi.org/10.1016/S0003-2670(02)01643-4, 2003.

Pernigotti, D., Belis, C. A., and Spanò, L.: SPECIEUROPE: The European data base for PM source profiles, Atmospheric Pollution Research, 7, 307–314, https://doi.org/10.1016/j.apr.2015.10.007, 2016.

Rai, P., Furger, M., Slowik, J. G., Canonaco, F., Fröhlich, R., Hüglin, C., Minguillón, M. C., Petterson, K., Baltensperger, U., and Prévôt, A. S. H.: Source apportionment of highly time-resolved elements during a firework episode from a rural freeway site in Switzerland, Atmospheric Chemistry and Physics, 20, 1657–1674, https://doi.org/10.5194/acp-20-1657-2020, 2020.

Reff, A., Eberly, S. I., and Bhave, P. V.: Receptor Modeling of Ambient Particulate Matter Data Using Positive Matrix Factorization: Review of Existing Methods, Journal of the Air & Waste Management Association, 57, 146–154, https://doi.org/10.1080/10473289.2007.10465319, 2007.

Sutresna, A., Keywood, M., Paton-Walsh, C., Simmons, J., Mynard, C., Dang, Q., Mochida, M., Ohata, S., Afsana, S., Kunwar, B., Kawamura, K., Humphries, R., Dunne, E., Ward, J., Harnwell, J., Reisen, F., Emmerson, K., Griffiths, A., Williams, A., Schofield, R., and Rayner, P.: Interference of sea salt in capture vaporizer-ToF-ACSM measurements of biomass burning organic aerosols in coastal locations, Environ. Sci.: Atmos., 4, 634–644, https://doi.org/10.1039/D3EA00171G, 2024.

Sylvestre, A., Mizzi, A., Mathiot, S., Masson, F., Jaffrezo, J. L., Dron, J., Mesbah, B., Wortham, H., and Marchand, N.: Comprehensive chemical characterization of industrial PM2.5 from steel industry activities, Atmospheric Environment, 152, 180–190, https://doi.org/10.1016/j.atmosenv.2016.12.032, 2017.

Tobler, A. K., Skiba, A., Wang, D. S., Croteau, P., Styszko, K., Nęcki, J., Baltensperger, U., Slowik, J. G., and Prévôt, A. S. H.: Improved chloride quantification in quadrupole aerosol chemical speciation monitors (Q-ACSMs), Atmos. Meas. Tech., 13, 5293–5301, https://doi.org/10.5194/amt-13-5293-2020, 2020.

Ulbrich, I. M., Canagaratna, M. R., Zhang, Q., Worsnop, D. R., and Jimenez, J. L.: Interpretation of organic components from Positive Matrix Factorization of aerosol mass spectrometric data, Atmospheric Chemistry and Physics, 9, 2891–2918, https://doi.org/10.5194/acp-9-2891-2009, 2009.

Via, M., Chen, G., Canonaco, F., Daellenbach, K. R., Chazeau, B., Chebaicheb, H., Jiang, J., Keernik, H., Lin, C., Marchand, N., Marin, C., O'Dowd, C., Ovadnevaite, J., Petit, J.-E., Pikridas, M., Riffault, V., Sciare, J., Slowik, J. G., Simon, L., Vasilescu, J., Zhang, Y., Favez, O., Prévôt, A. S. H., Alastuey, A., and Cruz Minguillón, M.: *Rolling* vs. *seasonal* PMF: real-world multi-site and synthetic dataset comparison, Atmos. Meas. Tech., 15, 5479–5495, https://doi.org/10.5194/amt-15-5479-2022, 2022.

Viana, M., Kuhlbusch, T. A. J., Querol, X., Alastuey, A., Harrison, R. M., Hopke, P. K., Winiwarter, W., Vallius, M., Szidat, S., Prévôt, A. S. H., Hueglin, C., Bloemen, H., Wåhlin, P., Vecchi, R., Miranda, A. I., Kasper-Giebl, A., Maenhaut, W., and Hitzenberger, R.: Source apportionment of particulate matter in Europe: A review of methods and results, Journal of Aerosol Science, 39, 827–849, https://doi.org/10.1016/j.jaerosci.2008.05.007, 2008.

Visser, S., Slowik, J. G., Furger, M., Zotter, P., Bukowiecki, N., Canonaco, F., Flechsig, U., Appel, K., Green, D. C., Tremper, A. H., Young, D. E., Williams, P. I., Allan, J. D., Coe, H., Williams, L. R., Mohr, C., Xu, L., Ng, N. L., Nemitz, E., Barlow, J. F., Halios, C. H., Fleming, Z. L., Baltensperger, U., and Prévôt, A. S. H.: Advanced source apportionment of size-resolved trace elements at multiple sites in London during winter, Atmos. Chem. Phys., 15, 11291–11309, https://doi.org/10.5194/acp-15-11291-2015, 2015.

Wang, D. S. and Ruiz, L. H.: Secondary organic aerosol from chlorine-initiated oxidation of isoprene, Atmos. Chem. Phys., 17, 13491–13508, https://doi.org/10.5194/acp-17-13491-2017, 2017.